

# Structure, Process, and Mechanism

Harald Sodemann, Heini Wernli, Peter Knippertz,  
Jason M. Cordeira, Francina Dominguez, Bin Guan,  
Huancui Hu, F. Martin Ralph, and Andreas Stohl

## 2.1 Introduction

This chapter describes the 3-dimensional (3-D) structure of ARs and explains the relevant processes and mechanisms involved in their formation, maintenance, and decay. This undertaking is ambitious because there are potential misconceptions about ARs, and, more fundamentally, because achieving a detailed understanding of AR dynamics is complex, given the many processes involved and their interactions. Misconceptions that require clarification include the following:

ARs transport tropical moisture toward the poles

Evaporation occurs in the entrance zone of an AR and precipitation near the exit

ARs replace the earlier concept of warm conveyor belts

In particular, Sects. 2.3 and 2.4 address these points by illustrating the complexity of the atmospheric water cyclone along ARs, and by comparing the AR concept to the alterna-

tive flow concepts of warm conveyor belts (WCBs) and tropical moisture exports (TMEs).

Section 2.2 first provides a concise description of ARs, including their definition and horizontal and vertical structure. The definition starts with “an AR is a long, narrow, and transient corridor of strong horizontal water vapor transport that is typically associated with a low-level jet (LLJ) stream ahead of the cold front of an extratropical cyclone ...” and includes elements about their geometry (long and narrow shape), their key characteristic (strong horizontal water vapor transport), and their dynamical embedding (LLJ ahead of an extratropical cyclone’s cold front).

Section 2.5 illustrates and explains in more detail these linkages to classical concepts of dynamical meteorology.

Overall, this chapter contains fairly technical discussions, but they serve to offer a more complete picture of the 3-D structure and transient nature of ARs; their relationship to cyclones, fronts, WCBs, and TMEs; as well as the complex interplay of AR dynamics with associated moisture transport and patterns of ocean evaporation and precipitation.

H. Sodemann  
Geophysical Institute, University of Bergen and Bjerknes Centre  
for Climate Research, Bergen, Norway  
e-mail: harald.sodemann@uib.no

H. Wernli  
Institute for Atmospheric and Climate Science, ETH Zürich,  
Zürich, Switzerland  
e-mail: heini.wernli@env.ethz.ch

P. Knippertz (✉)  
Institute of Meteorology and Climate Research, Karlsruhe Institute  
of Technology, Karlsruhe, Germany  
e-mail: peter.knippertz@kit.edu

J. M. Cordeira  
Plymouth State University, Plymouth, NH, USA  
e-mail: j\_cordeira@plymouth.edu

F. Dominguez  
University of Illinois, Urbana–Champaign, Champaign, IL, USA  
e-mail: francina@illinois.edu

B. Guan  
University of California, Los Angeles, Los Angeles, CA, USA  
e-mail: bin.guan@jpl.nasa.gov

H. Hu  
Pacific Northwest National Lab, Richland, WA, USA  
e-mail: huancui.hu@pnl.gov

F. M. Ralph  
Center for Western Weather and Water Extremes, Scripps  
Institution of Oceanography, University of California–San Diego,  
La Jolla, CA, USA  
e-mail: mralph@ucsd.edu

A. Stohl  
NILU - Norwegian Institute for Air Research, Kjeller, Norway  
e-mail: ast@nilu.no

## 2.2 Structure of ARs

This section provides a concise description of ARs, including their structure and how some of their key characteristics vary over many samples, as well as brief background on the origins of this information. The term's definition was developed for the *Glossary of Meteorology* in 2017 (Ralph et al. 2018). The definition includes a summary of the vertical and horizontal structure of ARs as informed by 21 aircraft-based measurements of ARs over the eastern North Pacific from several field campaigns (Ralph et al. 2017a). The representativeness of these difficult-to-collect observations—and the typical range of key AR characteristics across many samples—are summarized here based on a comparison of those 21 measurements with examination of several thousand ARs in reanalyses by Guan et al. (2018). (Reanalyses are gridded global meteorological data sets produced by numerical weather prediction centers based on all routinely available observations, to create a composite plan view.)

### 2.2.1 Definition of the Term “Atmospheric River”

The development of a formal definition was triggered by requests received by the GoM Editor from the meteorological community. These requests reflected a dramatic increase in publications that referred to the term, from 10 papers before 2004, to over 600 between then and 2016 (Ralph et al. 2017b). A process for community input was established. It included formation of a committee comprising four experts: including chairs of three standing American Meteorological Society (AMS) technical committees (mesoscale, hydrology, water resources) and the GoM Editor. The committee created a draft definition, building on a draft created earlier at the International Atmospheric Rivers Conference (IARC) in 2016—the first conference specifically addressing research on ARs. The draft was then discussed at two dedicated Town Hall meetings, one at the 2016 American Geophysical Union (AGU) Fall Meeting, and one at the 2017 AMS Annual Meeting. Each Town Hall included five or six diverse panelists who offered their opinions. Roughly 250 people attended these open forums, many of whom asked questions or offered comments. Because there had been diverse opinions about the appropriateness of the term “atmospheric river”—including how it related to the LLJ studied earlier (e.g., Browning and Pardoe 1973) and about what an “atmospheric river” was—the process of creating the definition was summarized in a brief article in the *Bulletin of the American Meteorological Society* (Ralph et al. 2018).

The committee settled on the following definition, which was then published in the GoM in May 2017: An atmospheric river is

a long, narrow and transient corridor of strong horizontal water vapor transport that is typically associated with a LLJ stream ahead of the cold front of an extratropical cyclone. The water vapor in atmospheric rivers is supplied by tropical and/or extratropical moisture sources. Atmospheric rivers frequently lead to heavy precipitation where they are forced upward, e.g., by mountains or by ascent in the warm conveyor belt. Horizontal water vapor transport in the mid-latitudes occurs primarily in atmospheric rivers and is focused in the lower troposphere.

### 2.2.2 Water Vapor Transport and the Vertical and Horizontal Structure of ARs

#### Direct Observations of Water Vapor Transport

Between 2005 and 2017, several field campaigns used research or weather reconnaissance aircraft to release dropsondes across ARs over the northeast Pacific during winter (Ralph et al. 2017a). The campaigns were “Ghost Nets” in 2005, “WISPAR” in 2011, “CalWater” in 2014 and 2015, and “AR Recon” in 2016. The National Oceanic and Atmospheric Administration (NOAA) P-3 and G-IV, National Aeronautics and Space Administration (NASA) Global Hawk, and Air Force C-130 aircraft were used. In each case, an aircraft flew at high altitude across an AR (Fig. 2.1), and released dropsondes—14 on average—at about a 100-km horizontal spacing over 1000–1500-km baseline across an AR. Dropsondes measured vertical profiles of water vapor, temperature, wind, and pressure with high vertical resolution as they descended to the ocean surface over 10–20 min. These data allowed calculation of vertically integrated water vapor (IWV) and vertically integrated water vapor transport (IVT). The campaigns were all in January, February, or March and spanned from roughly 20–50°N.

Each dropsonde transect across an AR could be used to calculate the width of the AR, its strength in terms of maximum IVT, and its total IVT (TIVT), which represents the total horizontal flux of water vapor in the AR, integrated horizontally from one edge of the AR to the other, and vertically from the surface to 300 hPa. Because the width and TIVT—which determines where an AR's edges are laterally—depend on the definition of an AR, many cases were analyzed to explore the relative importance of using IWV or IVT as a basis for defining an AR. (IWV was used initially because it was available directly from satellite; it was introduced by Ralph et al. 2004). Ralph et al. (2017a) showed just a few percent difference in width and TIVT in terms of the average of 21 cases. The use of IVT as the basis was also shown as most robust because at lower latitudes IWV sometimes never dropped below the standard

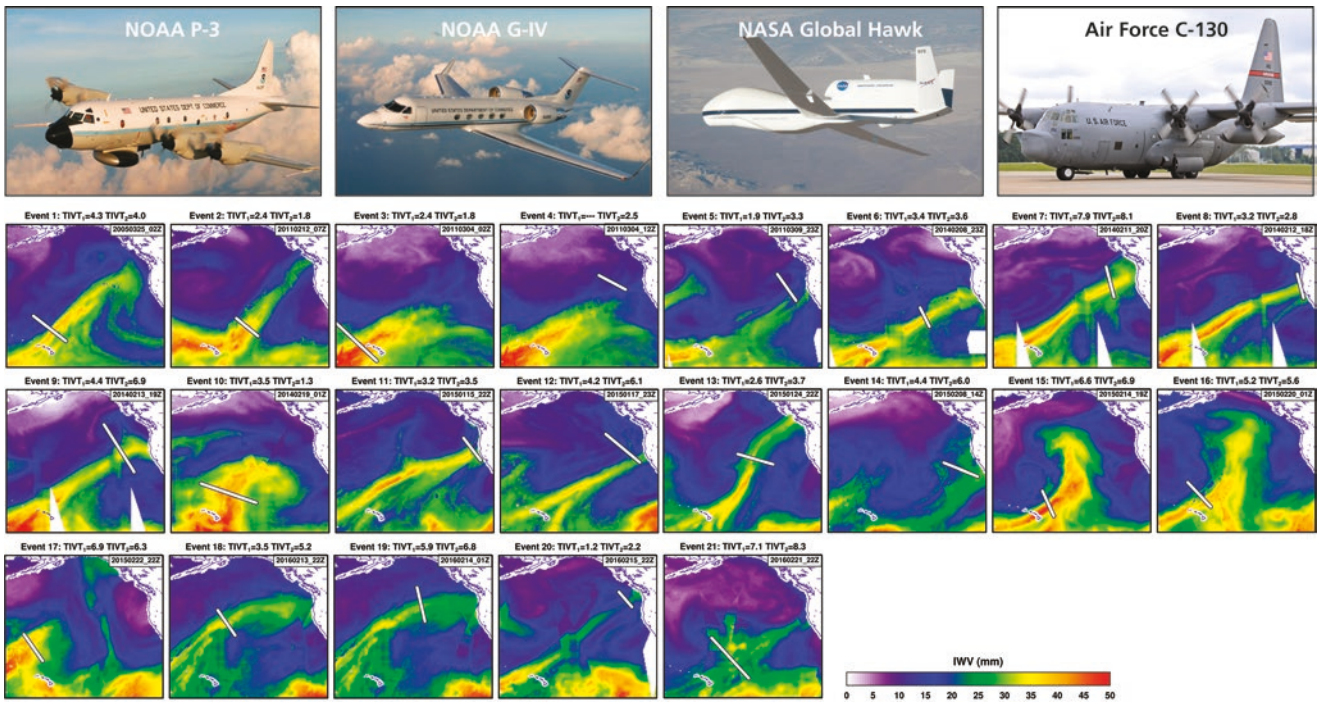


**Fig. 2.1** (Top row) Aircraft used in collecting dropsonde data between 2005 and 2016 to develop the observations-based composite of the cross-AR vertical structure (see Fig. 2.2). (Bottom rows) Satellite images of vertically integrated water vapor (IWV) including the AR

transect baseline for each of the flights used in the study. The values of TIVT ( $\times 10^8 \text{ kg s}^{-1}$ ) are shown as text atop each IWV panel for each case based on both the IWV (*subscript 1*) and IVT (*subscript 2*) AR threshold methods. (Adapted from Ralph et al. 2017a)

2-cm threshold, although IVT did. Also, at higher latitudes, some ARs were well defined by IVT, but, because the air was cooler than at lower latitudes, IWV sometimes remained below the 2-cm threshold. Not only is IVT more robust as a basis, it is a more appropriate parameter than IWV for a phenomenon focused on horizontal water vapor transport. Thus, keeping in mind that shape requirements (e.g., long and narrow) are often used in addition to the IVT threshold, and that researchers have had success using a variable IVT threshold that is scaled to local climatology and varies with season,  $\text{IVT} = 250 \text{ kg s}^{-1} \text{ m}^{-1}$  was recommended as the most useful threshold for defining an AR (as also used in Sect. 2.1).

A key result of the compositing and comparisons was the conclusion that an average AR is roughly  $850 \pm 250 \text{ km}$  wide, and transports  $4.7 \pm 2.0 \times 10^8 \text{ kg s}^{-1}$  of water vapor, equivalent to roughly 25 times the Mississippi River's (or 2.5 times the Amazon River's) discharge into the ocean.

### Observations of Vertical and Horizontal Structure

The dropsonde transects were then used to create a composite vertical cross-section and combined with reanalysis data to create a composite plan view. These are shown in Fig. 2.2. To create the composite, the center point of each AR was identified as the position of maximum IVT. Each AR was

then adjusted in terms of position and orientation to enable spatial compositing.

Figure 2.2a shows that ARs are typically centered over 1000 km from their parent extratropical cyclone (L), and their position is aligned with and overlaps the cold front and trailing stationary front. The AR intersects the warm front, but is depleted through precipitation from ascent in the warm conveyor belt (WCB; e.g., Madonna et al. 2014). The average maximum value of IVT is  $700 \text{ kg s}^{-1} \text{ m}^{-1}$ . The vertical structure is shown in Fig. 2.2b and shows its position relative to the jet-front system and tropopause, including an upper-level jet of over  $60 \text{ m s}^{-1}$  and a LLJ of about  $30 \text{ m s}^{-1}$ . Although upper-level winds are roughly twice as strong as the LLJ, the air is cold and dry at high altitudes. The water vapor mixing ratio in the LLJ averages over  $9 \text{ g kg}^{-1}$ , roughly 10 times the value in the upper jet. The result is that water vapor flux is focused in the lower troposphere, with roughly 75% of IVT located below 3 km mean sea level (MSL), and <1% occurring in the upper jet (i.e., above about 400 hPa or 8 km MSL; Ralph et al. 2017a).

The plan-view composite (Fig. 2.2a) includes IWV, which shows an anomaly of large IWV extending from lower (closer to the equator) latitudes into the AR, a feature that is evident in the IWV fields shown in Fig. 2.2 for each AR. Although the composite IVT does not show a clear connection to the lower latitudes, the IWV signature may

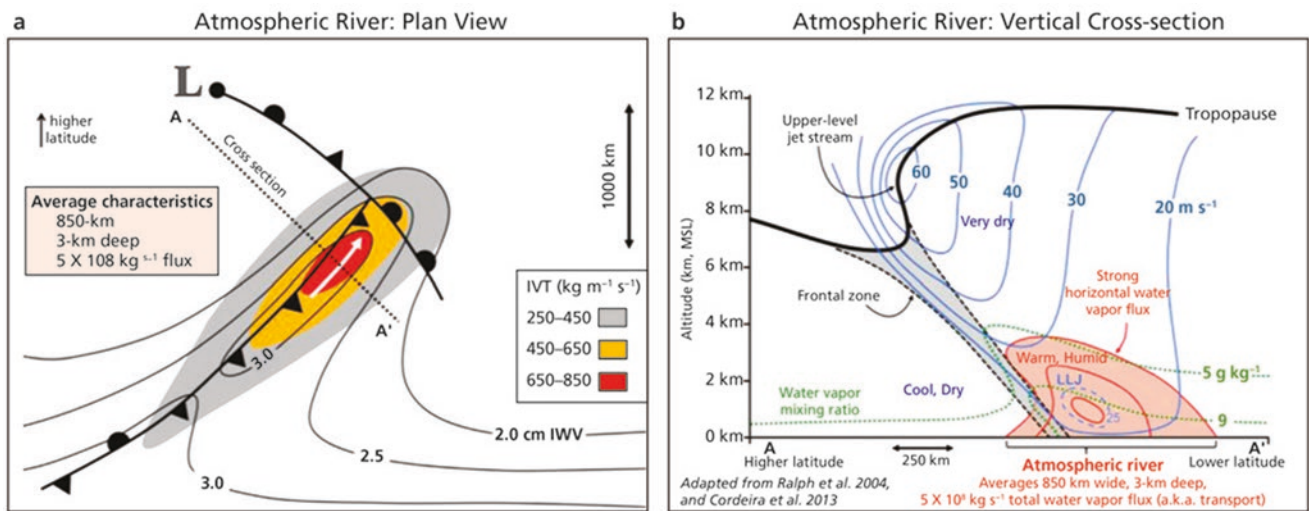


**Fig. 2.2** Schematic summary of the structure and strength of an AR based on dropsonde measurements deployed from research aircraft across many ARs, and on corresponding reanalyses that provide the plan-view context. Magnitudes of variables represent an average mid-latitude AR. Average width is based on AR boundaries defined by vertically integrated water vapor transport (IVT; from surface to 300 hPa) lateral boundary threshold of  $250 \text{ kg m}^{-1} \text{ s}^{-1}$ . Depth corresponds to the altitude below which 75% of IVT occurs. The total water vapor transport (AKA flux) corresponds to the transport along an AR, bounded laterally by the positions of  $\text{IVT} = 250 \text{ kg m}^{-1} \text{ s}^{-1}$ , and vertically by the surface and 300 hPa. (a) Plan view including parent low pressure system, and associated cold, warm, stationary, and warm-occluded surface

fronts. IVT is shown by *color fill* (magnitude,  $\text{kg m}^{-1} \text{ s}^{-1}$ ) and direction in the core (*white arrow*). Vertically integrated water vapor (IWV, cm) is *contoured*. A representative length scale is shown. The position of the cross-section shown in panel (b) is denoted by the *dashed line A-A'*. (b) Vertical cross-section perspective, including the core of the water vapor transport in the AR (*orange contours and color fill*) and the pre-cold-frontal low-level jet (LLJ), in the context of the jet-front system and tropopause. Water vapor mixing ratio (*green dotted lines*,  $\text{g kg}^{-1}$ ) and cross-section-normal isotachs (*blue contours*,  $\text{m s}^{-1}$ ) are shown. (From Ralph et al. (2017a), including elements from Cordeira et al. (2013) and others; Schematic prepared by F. M. Ralph, J. Cordeira, and P. J. Neiman)

represent a link to TMEs (e.g., Knippertz et al. 2013) that are characterized by poleward transport of tropical water vapor into the extratropics. Although many ARs can form without a tropical connection, it is clear that in some cases an AR can entrain significant water vapor from the tropics (e.g., Sodemann and Stohl 2013), and that this entrained water vapor may largely be rained out before reaching mid-latitudes (e.g., Cordeira et al. 2013)

### Representativeness of Airborne Observations and Typical Range of Key Characteristics

As much as the 21 aircraft-observed ARs represent a solid basis for calculating the mean and creating a composite, examining many more ARs would be helpful. This would help document the fuller range of AR conditions, as well as the representativeness of the 21 ARs. However, this was impractical in terms of aircraft, so Guan et al. (2018) turned to the European Centre for Medium-Range Weather Forecasts (ECMWF's) European Reanalysis (ERA)-Interim and Modern-Era Retrospective Analysis for Research and Application (MERRA)-2 reanalysis products. This allowed examination of ARs in the northeast Pacific during January–March each year from 1979 to 2016, including the cases documented by aircraft in Ralph et al. (2017a).

Guan et al. (2018) used the AR Detection Method (ARDM) Guan and Waliser (2015) developed, which uses a spatially-variable IVT threshold that represents the 85th to 95th percentile of IVT observed at a given grid cell in the reanalysis product. The threshold is also allowed to vary by season. AR “objects” then must meet shape requirements in terms of length and length-to-width ratio. The ARDM identified almost 6000 ARs during this period and in this large area. Figure 2.3a, b shows the spectrum of AR widths and AR TIVTs for these ARs.

The mean width of all ~6000 ARs in the reanalysis was 847 km. The mean of the reanalysis version of the 21 aircraft cases was 868 km. Both are remarkably close (within 2–5%) to the value of 886 km from the 21 aircraft observations. Similarly, the mean TIVT of all ~6000 ARs in the reanalysis was  $4.49 \times 10^8 \text{ kg s}^{-1}$ . The mean of the reanalysis version of the 21 aircraft cases was  $4.86 \times 10^8 \text{ kg s}^{-1}$ . Both are remarkably close (within 5–10%) to the value of  $4.71 \times 10^8 \text{ kg s}^{-1}$  from the 21 aircraft observations. These similarities are even more remarkable in that they used significantly different methods than in Ralph et al. (2017a, b). This agreement between aircraft observations and reanalyses adds robustness to the mean AR widths and TIVTs presented in Fig. 2.2 for the northeast Pacific in January–March.

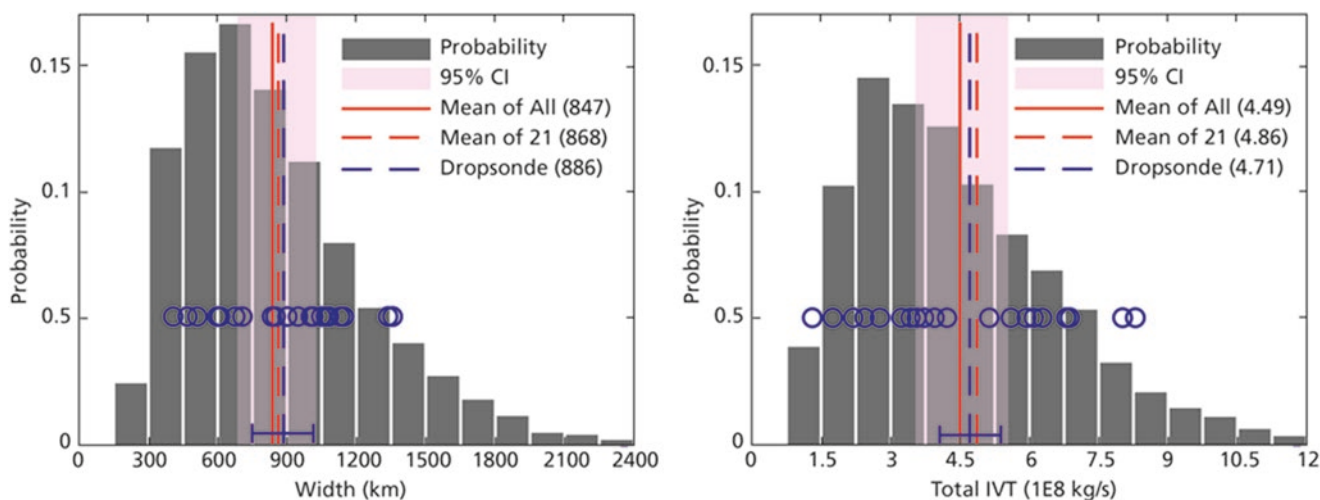


**Fig. 2.3** (left) Frequency of occurrence of AR widths based on ERA-Interim and MERRA2 reanalysis data using the Guan and Waliser (2015) ARDT applied to the northeast Pacific basin in January–March each year from 1979–2016. Means are shown of all ~6000 ARs (*solid red line*), the reanalysis representations of the 21 aircraft-observed ARs

(*dashed red line*), and the aircraft observations (*dashed blue line*). The 95% confidence range for the mean is shown (*red shading*), as is the distribution of the actual aircraft-measured cases (*blue circles*). (right) Same as (left), but for TIVT (Guan et al. 2018)

### 2.3 WCBs and TMEs and Their Relationship to ARs

In the meteorological literature, different concepts exist that describe meso- to synoptic-scale filamentary features of enhanced absolute moisture content or moisture transport (sometimes vertically integrated), clouds, and precipitation. In addition to ARs, these include WCBs, moisture conveyor belts, moisture bursts, TMEs, tropical plumes, and tropical intrusions (see, e.g., Knippertz (2007) for an overview of the tropical phenomena). These concepts—usually promoted by different research groups—deviate from each other by emphasizing different meteorological aspects. For some of these features, clear objective identification criteria exist, but others are more loosely defined phenomenologically. Naturally, the boundaries between these concepts are not sharp, leading—at least partly—to coincidences in time and space or temporal succession of features. The emphasis on different meteorological parameters leads to differing geographical, seasonal, and inter-annual variations in the frequency of these features.

This multitude of concepts and the lack of sharp boundaries and systematic comparisons have led to a certain level of confusion in the scientific community about each concept’s specific definition, purpose, and usefulness. This section focuses on two concepts that have explicitly been linked to ARs in past literature and for which objective identification methods exist: WCBs and TMEs.

TMEs consist of trajectories characterized by an intense horizontal export of tropical moisture into subtropical and mid-latitudes.

WCBs are trajectories with a strong ascent in the vicinity of extratropical cyclones and their fronts.

Excluded are other concepts that mostly rely on cold clouds identified from infrared satellite imagery, such as tropical plumes; they often occur at upper-tropospheric levels only, and their identification is sensitive to the satellite data set used (Fröhlich et al. 2013). This section:

1. portrays the key characteristics of the three concepts: AR, WCB, and TME—and how they are objectively identified (including a short illustrative case study)
2. quantifies how often the three features partially overlap in space and time (including a comparison of global climatologies for the two solstice seasons and statistical linkages between them)
3. provides a physical interpretation of the findings

All analyses are based on 6-hourly ERA-Interim reanalysis data (Dee et al. 2011) for the time-period 1979–2014 interpolated to a regular  $1^\circ$ -by- $1^\circ$  grid with 60 vertical levels. By systematically clarifying and quantifying the relationship of ARs to TMEs and WCBs for the first time, the key characteristics of ARs can be better understood.

#### 2.3.1 Concepts of TMEs, ARs, and WCBs

The TME concept was developed between 2005 and 2010 on the basis of a number of case studies. Knippertz and Martin (2005) analyzed three unusual boreal winter rainfall events in northern Africa associated with tropical cloud plumes, using trajectories to demonstrate the anticyclonic inflow of

moisture from the tropics ahead of an upper-level trough. Bao et al. (2006) presented a study on enhanced IWV bands associated with extratropical cyclones, in which they suggested the term “moisture conveyor belt” as an alternative to AR to better link with the more established WCB concept. They also used trajectories to show the involvement of tropical moisture in some of the cases investigated. The terminology of “moisture conveyor belts” was then also used to analyze precipitation events in the southwestern USA by Knippertz and Martin (2007), and in Norway by Stohl et al. (2008), but usage since then has been sparse.

Inspired by these and some other results, Knippertz and Wernli (2010) developed an objective trajectory-based identification and climatology for significant moisture transports from the tropics to higher latitudes on synoptic time-scales, which they termed TMEs. Knippertz et al. (2013) updated and expanded the climatology to the Southern Hemisphere. Figure 2.4a schematically illustrates a basic TME. One-day forward trajectories are calculated daily, starting at 0000 UTC from every  $100 \times 100 \text{ km} \times 30\text{-hPa}$  box within the tropical belt ( $20^\circ\text{S}$ – $20^\circ\text{N}$ ) and between 1000 and 490 hPa. Out of the  $\sim 300,000$  trajectories per day, only those that cross  $20^\circ\text{N}$  or  $20^\circ\text{S}$  are continued for another 6 days. Trajectories that reach a water vapor flux of at least  $100 \text{ g kg}^{-1} \text{ m s}^{-1}$  somewhere poleward of  $35^\circ$  latitude are defined as TME trajectories. Every trajectory represents the same atmospheric mass of  $\sim 3 \times 10^{12} \text{ kg}$ , and thus specific humidity interpolated along

the trajectories can be readily converted into water mass. Note that it is possible that some of the moisture that contributes to the intense water vapor flux at  $35^\circ$  latitude has been acquired poleward of the tropics from ocean evaporation. However, since most of the TME trajectories leave the tropical belt above the boundary layer (Knippertz and Wernli 2010), most of the TME moisture is most likely of tropical origin.

In addition to the actual climatologies of TME trajectory counts and associated water vapor transport, Knippertz and Wernli (2010) and Knippertz et al. (2013) analyzed the inter-annual variability of TMEs and its association with El Niño. The former paper also analyzed climatological contributions to precipitation in the extratropics, which reaches up to 60% over the North Pacific in boreal summer; the latter shows that, statistically, 90% of the ARs reaching the west coast of North America during December to May are connected to TMEs. Recently, the TME concept has been used to analyze precipitation in France (Lu et al. 2013) and in North America (e.g., Steinschneider and Lall 2016).

ARs, their history, and structure are explained in detail elsewhere in this book (Chap. 1 and, in particular, Sect. 2.1 earlier in this chapter). Here, a quantitative definition of ARs has been implemented that was agreed upon as “reasonable” at the 2015 AR workshop at the University of California, San Diego’s Scripps Institution of Oceanography (UCSD Scripps), and which is broadly consistent with the range of

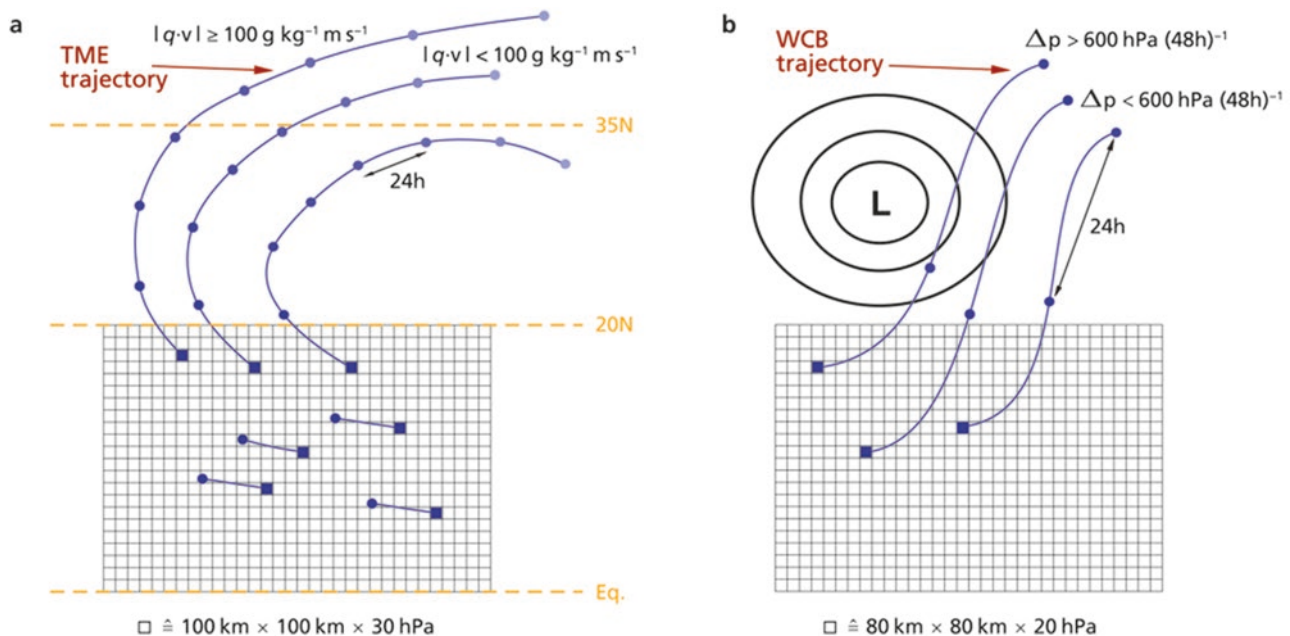


**Fig. 2.4** Schematic depiction of the objective identification algorithms for (a) TMEs and (b) WCBs. Blue lines show example trajectories started from pre-defined 3-D atmospheric volumes marked by blue boxes with 24-h periods marked by blue circles. (a) To classify as TME, trajectories need to start equatorward of  $20^\circ$  latitude and reach a water

vapor flux of at least  $100 \text{ g kg}^{-1} \text{ m s}^{-1}$  somewhere poleward of  $35^\circ$  latitude (example for Northern Hemisphere is shown here). (b) WCB trajectories need to cross the objectively identified area of a cyclone and ascend by more than 600 hPa in 48 h. (Panel (a) is modified from Fig. 2 in Knippertz and Wernli 2010)

methods used in the literature and with the general GoM description of ARs given in Sect. 2.2.1. It is as follows:

In contrast to TMEs and WCBs, a Eulerian approach to define ARs is used here: ARs are identified here as 2-dimensional (2-D) objects poleward of  $20^\circ$  latitude with length scales of at least 2000 km. Every grid point in this object fulfills the criteria that (1) IWV is larger than  $20 \text{ kg m}^{-2}$  (equivalent to 20 mm), and (2) IVT is larger than  $250 \text{ kg m}^{-1} \text{ s}^{-1}$ .

According to this definition, ARs are typically, but not always, filamentary synoptic-scale features of both enhanced moisture and strong horizontal moisture transport. Conceptually, ARs differ from TMEs mainly because ARs need not contain moisture of tropical origin, and they focus on vertically coherent structures; whereas, in principle, a TME can be shallow with intense moisture transport only at a particular level.

In contrast to ARs and TMEs, WCBs have a history that can be traced back for longer than a century. Central to WCBs is the idea of coherent air flows in extratropical cyclones. Despite the chaotic nature of atmospheric flows, early synoptic analyses and later satellite imagery revealed the impression that cyclones are characterized by coherent poleward-moving air streams of warm and moist air. Shaw and Lempfert (1906) showed very early illustrations of surface air-parcel trajectories calculated from synoptic weather maps. Decades later, Rossby and Namias pioneered the concept of isentropic analyses and considered the motion of moist and dry air masses on sloping isentropes over the USA (e.g., Rossby et al. 1937). Green et al. (1966) then used moist isentropes to identify zones of saturated ascent along cold fronts. They emphasized that in certain situations subtropical air masses from the Caribbean Sea may rise over a front into the jet stream. Browning and Harrold (1969) in the UK, and later Carlson (1980) in the USA, noted the usefulness of these air streams for understanding the precipitation pattern in extratropical cyclones. Browning (1971) was the first to use the term WCB to denote these moist ascending and precipitation-producing air streams. Since the work by Rossby et al., the ascent of moist air was an essential aspect of what was later termed as WCB, in contrast to ARs and TMEs, which primarily emphasize the horizontal moisture transport. Clearly, the ascent of WCBs leads to condensation, and the formation of clouds and precipitation, and this is why Browning (1990) stated that WCBs are the primary source of precipitation in extratropical cyclones.

With the advent and subsequent availability of reanalysis data, validating the concept of coherently ascending air streams with trajectory calculations became possible. Wernli and Davies (1997) defined WCBs as strongly ascending trajectories in the vicinity of extratropical cyclones and used a criterion of 600-hPa ascent within 2 days (see Fig. 2.4b). They showed that the strong ascent goes along with intense latent heating (typically 20 K over the 2 days) and precipita-

tion, consistent with Browning's earlier definition. Since then, WCBs have been objectively identified by calculating very large numbers of trajectories and selecting those that fulfill the ascent criterion (e.g., to produce WCB climatologies; Stohl 2001; Eckhardt et al. 2004; Madonna et al. 2014). In recent years, WCBs have been shown to be highly relevant for the dynamics of upper-tropospheric Rossby waves and anticyclonic blockings (e.g., Grams et al. 2011; Pfahl et al. 2015), and to be associated with a complex microphysical evolution from warm-phase clouds in the WCB inflow to cirrus clouds in the WCB outflow (Joos and Wernli 2012).

### 2.3.2 Climatologies

All three features (TMEs, ARs, and WCBs) have 2-D fields of occurrence frequency constructed every 6 h for ERA-Interim climatologies for the December–January–February (DJF) and June–July–August (JJA) seasons. For each feature, a value of 1 is assigned to grid points that belong to this feature, and a value of 0 to all other grid points. In this way, simple time averaging of these binary fields leads to climatological frequency fields. For instance, an averaged value of 0.2 indicates that at this grid point the feature occurs in 20% of all time instants. The calculation of the 6-hourly binary fields is straightforward for the ARs: a value of 1 is simply attributed to all grid points that fulfill the AR criteria set out in the previous section. For TMEs and WCBs, which are trajectory-based features, binary fields are constructed by asking: *for every 6-hour time-step and for every  $1^\circ$ -by- $1^\circ$  grid column, is at least one 5-day TME trajectory or 2-day WCB trajectory present?* For these Lagrangian features, a climatological frequency value of 20% indicates how often at least one trajectory of the considered category is somewhere in the vertical column represented by the grid point—but it does not provide information about how many TME or WCB trajectories are present. Similarly, the AR frequencies just indicate how often the criteria are met, but not how far they are exceeded. Given the criteria outlined above, TMEs and ARs are only defined outside the  $20^\circ\text{S}$ ,  $20^\circ\text{N}$  tropical belt, which can lead to sharp gradients in the frequency diagrams at  $20^\circ$  latitude.

The information provided here complements to some extent the more detailed climatologies presented in Knippertz and Wernli (2010) and Knippertz et al. (2013) for TMEs, and Madonna et al. (2014) for WCBs. For ARs, many more aspects of their climatology and effect on heavy precipitation are discussed in other parts of this book. Climatologies of TMEs, ARs, and WCBs are calculated for the first time here with the same underlying data set and compared directly to one another.

The resulting plots of the frequency of occurrence (hereafter just frequencies) for all three features are shown in Fig. 2.6

for the solstice seasons DJF (left) and JJA (right). In boreal winter, TMEs in the Northern Hemisphere show two clear occurrence maxima: one over the central–eastern North Pacific and one over the western Atlantic (Fig. 2.6a). Values are largest in the subtropics and then stretch across the mid-latitude parts of the ocean basin, finally reaching the adjacent continents: North America and Europe (respectively termed “Pineapple Express” and “Gulf Stream” in Knippertz and Wernli 2010). Mid-latitude maxima reach values of about 30%, although near-20°N frequencies of more than 60% are found. In the Southern Hemisphere, overall values are larger, and two strong maxima are found again over the Pacific and Atlantic, with the latter particularly pronounced just off the coast of Brazil (Fig. 2.6a). These are associated with the South Pacific and South Atlantic Convergence Zones, respectively. Weaker maxima occur east of South Africa near Madagascar and over Western Australia (see also Knippertz et al. 2013). For JJA, patterns in the Southern Hemisphere change rather little but overall values decrease, although activity shifts into the South American continent and over southern Africa (Fig. 2.6b). In the Northern Hemisphere in contrast, dramatic seasonal changes are revealed. The maximum over the Pacific shifts westward to the Asian coast, reaching the largest values of any region and season of more than 70%. Only a small fraction of TME trajectories reach the North American continent during this season. In the Atlantic sector, a sharp narrow band of TMEs connects the Caribbean and the Gulf of Mexico with the US Great Plains, although the “Gulf Stream” maximum is strongly reduced in zonal extent compared to DJF.

The climatology of ARs (Fig. 2.6c, d) shares a number of similarities with the TME occurrence frequencies, despite the overall somewhat smaller frequencies. There are geographical matches for most of the maxima discussed for TMEs above, but AR maxima tend to be more elongated—mostly in the WSW–ENE direction in the Northern Hemisphere and in the WNW–ESE direction in the Southern Hemisphere, respectively—and therefore generally have larger values farther away from the equator, relatively speaking. Given the strong emphasis on moisture and moisture transport, both TMEs and ARs tend to show larger values in the summer hemispheres. (This seasonality aspect will be discussed further in Sect. 2.3.4.) The most striking differences between the two features are: (1) the relatively weak AR signature over the North American Great Plains in summer and over South America in winter (Fig. 2.6d) and (2) AR maxima aligned along 20°N during Northern Hemisphere summer (Fig. 2.6d). The former is most likely a consequence of the length criterion used in the AR definition, which filters out those TMEs where trajectories ascend and moisture condenses and rains out at relatively low latitudes. The latter is related to the warm sea-surface temperatures over the western Atlantic, Indian Ocean, and West Pacific, which allow for enhanced atmospheric moisture contents in combination with relatively stable circulations associ-

ated with the Asian and American monsoon systems. This type of AR, which is aligned westward with the trade winds, has not been discussed in the literature.

Another remarkable difference between the AR and the TME climatologies is the large seasonal cycle in areas around South Africa and Australia (cf. Fig. 2.6c, d). This points to a substantial reduction in moisture here from summer to winter, which in the TME climatology may be compensated for by an increase in meridional transport (Fig. 2.6a, b), but this requires further study to be confirmed. Also noteworthy is that ARs as defined here show hardly any penetration into the North American continent from the west in both seasons (e.g., Rutz et al. 2014, 2015), which is probably related to the strong rain-out of moisture by the steep and high topography close to the coast. For Europe, penetration is weak in winter, but reaches far into Russia in summer, which contrasts with TMEs, where the restriction to 5-day trajectories and the weaker summertime flow does not allow an extension that far to the northeast from the main sources.

Finally, the climatology for WCBs is given in the bottom panels of Fig. 2.6. Compared to the other two features, WCBs show a significantly larger extension into higher latitudes. Given the emphasis on vertical motion—and, therefore, storm dynamics—there is a tendency toward greater frequencies in winter, in contrast to the other two features with their emphasis on moisture and largest frequencies in summer.

In Northern Hemisphere winter, there is qualitative agreement in the location of the two maxima of WCBs in the Atlantic and Pacific storm track areas (Fig. 2.6e) with the climatologies of TMEs and ARs (Fig. 2.6a, c). However, in summer, contrasts among the three features are stark, with generally much lower frequencies of WCBs and no Great Plains maximum (Fig. 2.6f). The weak summertime maximum of WCBs over Asia is related to strong orographic ascent caused by monsoonal meridional flow toward the Himalayas. All three features agree, at least, that in JJA the Pacific storm track is more active than its counterpart in the Atlantic. In JJA, the locations of the North Pacific maxima of WCBs, TMEs, and ARs are remarkably similar; which is in line with the large contribution of tropical moisture sources for North Pacific WCBs in summer (see Fig. 3 in Pfahl et al. 2014).

In the Southern Hemisphere, activity maxima in the areas of the South Pacific and South Atlantic Convergence Zones agree well among the three features in terms of geographical position, but not in magnitude. The maximum off the coast of South America shows some agreement with the respective maximum in TME frequency, but, for WCBs, the maximum is extended southeastward in JJA. Contrasts to ARs are, again, large. For the Australian region, WCB activity is concentrated to the southeast and southwest of the continent, similar to ARs but in contrast to TMEs. Differences in WCB activity are small between summer and winter, again in stark contrast to

ARs. The implication here is that baroclinic instability (i.e., extratropical cyclogenesis) remains active at about the same level year-round in the Southern Hemisphere, whereas in the Northern Hemisphere it is most prominent in winter.

### 2.3.3 Linkages Among the Three Feature Categories

Both the case study (Fig. 2.5) and climatologies (Fig. 2.6) reveal an interesting and rather complex relationship among the three features. Moisture-transport events simultaneously fulfill the criteria of ARs, TMEs, and WCBs; however, more often it appears that the three feature categories emphasize different aspects of the flow and/or different events. Here, this linkage is quantified in detail, again making use of the 6-hourly 2-D fields of AR, TME, and WCB occurrence. For the Northern Hemisphere winter and summer seasons and the region poleward of 20°N, every 6 hours the areas where (1) none of the features is present, (2) where one of them occurs in isolation, and (3) where two or all three of them overlap are determined. The seasonal mean values (in % of the area poleward of 20°N) are then displayed in the form of a Venn diagram in Fig. 2.7.

Focusing first on ARs in winter, the sum of the four values in the red circle in Fig. 2.7a indicates that, on average, 6.71% of the area was covered by an AR. Often, ARs occur in isolation (2.65% of the area, corresponding to about 40% of all ARs). In a similar number of cases (2.51%), ARs co-occur with TMEs but not WCBs. About 23% of all ARs overlap with WCBs, split almost evenly into occasions with (0.79%) and without (0.76%) additional occurrence of TMEs. Similarly, the values in the green and blue circles provide information about TMEs and WCBs, respectively, and their overlap with

other features. In agreement with Fig. 2.6, the overall frequency of TMEs (11.7% of the area) is larger than that of ARs, while the frequency of WCBs is smaller (5.85% of area). The most frequent overlap is between ARs and TMEs, which again agrees with the similarity of their climatological distributions (Fig. 2.6a, b). TMEs and WCBs occur more often in isolation than with a mutual overlap. Coincidences of all three features are relatively rare (0.79% of the area), which in relative terms indicate that this situation occurs for about 12% of all ARs, 7% of all TMEs, and 14% of all WCBs, respectively.

In Northern Hemisphere summer (Fig. 2.7b) some values change strongly compared to winter, in agreement with the climatologies shown in Fig. 2.6. ARs become more frequent, now covering 17.05% of the area, TMEs have a similar overall frequency (11.04% of the area), and WCBs become less frequent (only 2.4% of the area). Most of the ARs (61%) occur in isolation, although in summer 50% of all TME grid points coincide with ARs. The overlap between ARs and TMEs is again the most frequent type, even more strongly than in winter. Interestingly, despite the strong seasonality of the AR and WCB frequencies and the geographical distributions of all three features, the frequency of 3-fold coincidence is almost the same in summer as in winter (0.73% and 0.79% of the area, respectively). In summer, this means that only slightly more than 4% of all ARs simultaneously overlap with both TMEs and WCBs, and 32% of all ARs overlap with a TME only. The interpretation is that most ARs do not have a tropical origin (in particular the ones over the North Atlantic, cf. Fig. 2.6b, d) and that only a few of them are characterized by the strong ascent required for WCBs. The first of these results is in line with the findings of Dacre et al. (2015), who composited the moisture budget for 200 intense extratropical cyclones and found that local sources of water vapor are essential for the formation and

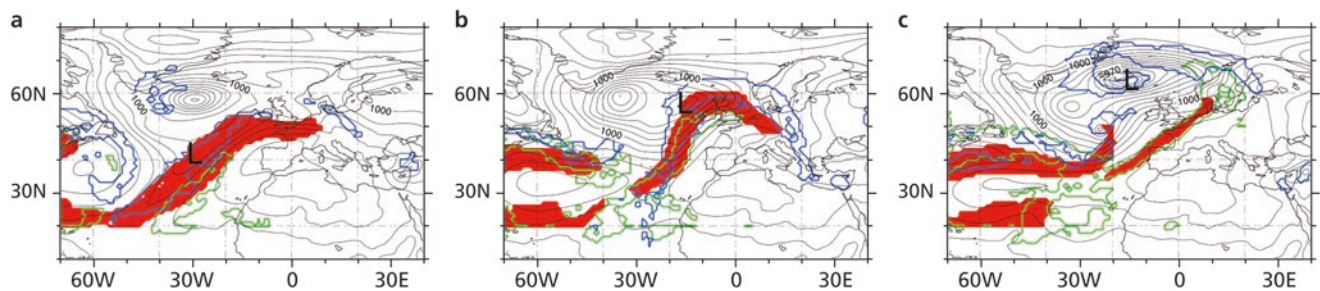


**Fig. 2.5** Illustrative case study of a North Atlantic cyclone (position marked with label “L”) at (a) 0000 UTC 22 Nov, (b) 0000 UTC 23 Nov, and (c) 0000 UTC 24 Nov 1992. Black contours show mean sea-

level pressure (in hPa), red shading marks the identified ARs, and green and blue contours are the identified TMEs and WCBs, respectively

<sup>1</sup>It is important to note that this percentage value (and similar values of overlap mentioned below) refers to grid points (and not entire features); i.e., 23% of all AR grid points are at the same time also WCB grid points. Such an overlap value results if, for instance, a full overlap

occurred for 23% of all ARs, or if for every AR there was a 23% areal overlap with a WCB. Very likely, there is large variability, with few AR features having an almost perfect overlap with WCBs (see, e.g., Fig. 2.5a) and others with almost no overlap (e.g., Fig. 2.5c).

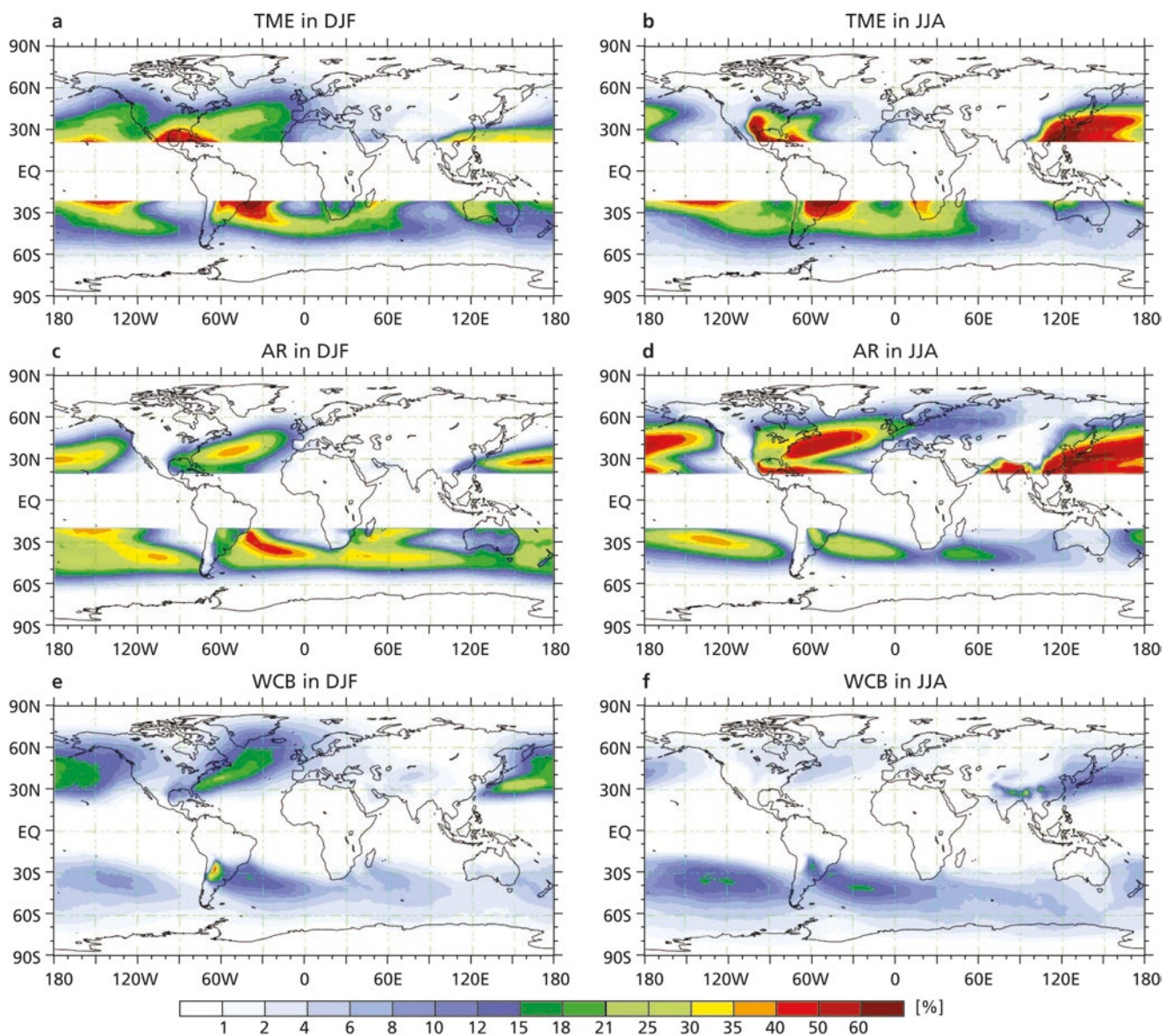


**Fig. 2.6** Climatological frequencies (in %) of TMEs (a, b), ARs (c, d), and WCBs (e, f), derived from ERA-Interim data for the time-period 1979–2014. Left-hand panels show boreal winter (DJF); right-hand

panels show boreal summer (JJA). See text for exact definitions of the three features

maintenance of the large IWV values in the cyclone’s warm sector, which are characteristic of ARs. Similar conclusions were reached in the detailed case studies by Bao et al. (2006), and Sodemann and Stohl (2013)—see also Sect. 2.4.

### 2.3.4 Summary

For the first time, climatologies of all three features (ARs, TMEs, and WCBs) have been derived from the same global reanalysis data set, enabling comparison of the seasonality of their geographical frequency patterns, and the statistics of their overlap. The main results can be summarized as follows:

- The three features reveal a different and asynchronous seasonality: ARs are more frequent in summer, WCBs in winter, and TMEs have a weak seasonality with a peak in summer (considering hemispherically integrated frequencies). This reflects the generally enhanced vertically integrated humidity values in the warm season (which is beneficial for the formation of ARs) and the stronger baroclinicity and large-scale forcing for ascent in the cold season (which is beneficial for the formation of WCBs). For TMEs, it appears that the enhanced moisture values in summer and the stronger low-level winds in winter lead to the fairly flat seasonal cycle. For specific regions, seasonality can be pronounced, e.g., the very strong frequency

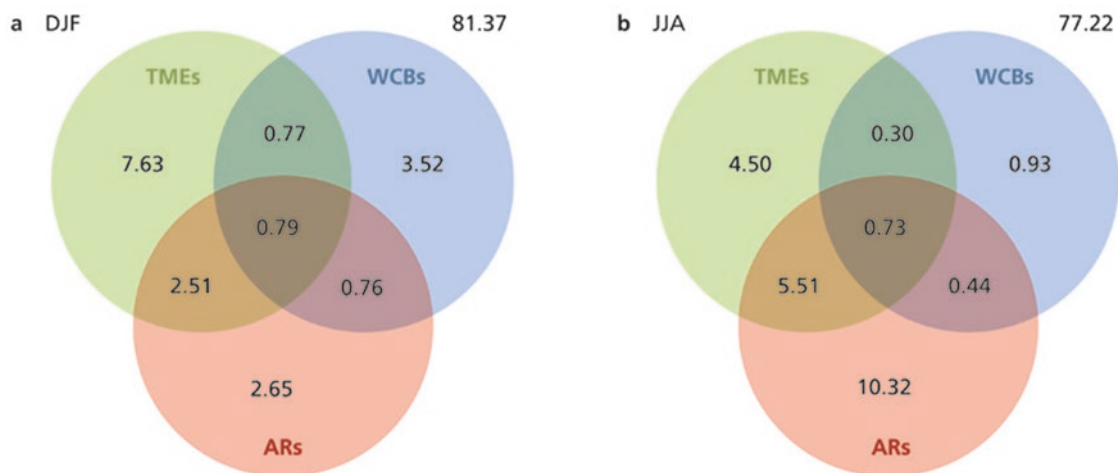


**Fig. 2.7** Venn diagrams for (a) boreal winter (DJF) and (b) boreal summer (JJA), showing the percentage of area in the Northern Hemisphere extratropics (north of 20°N) that is, on average, covered by

ARs, TMEs, and WCBs only and simultaneously by two or three of the features. The value in the *top right* of each panel indicates that, on average, about 80% of the area is not covered by any of the three features

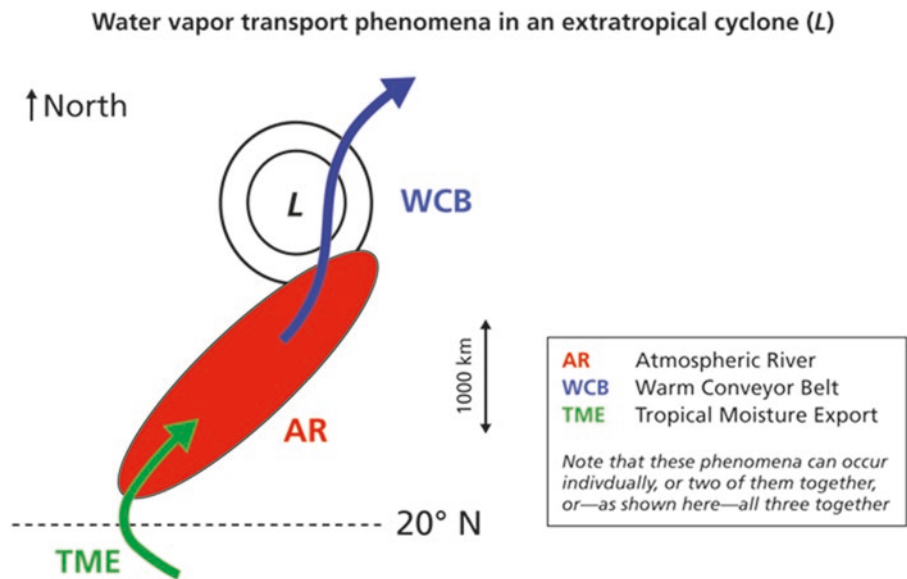
maximum of TMEs in summer over the US Great Plains and the western North Pacific, and a maximum of AR frequencies near the US West Coast in winter. WCBs typically occur further poleward than TMEs and ARs, in agreement with their ascent in the main mid-latitude baroclinic zone. It is important to critically comment on the seasonality of ARs in this section. The use of geographically and temporally uniform AR selection criteria (fixed thresholds for IWV, IVT, and length) together with the higher humidity content in mid-latitudes in summer leads to a clear summer maximum in the frequency of ARs in most parts of the globe (cf. Fig. 2.6c, d) and very large frequencies of more than 60% south of Japan. (Note also that in this region the frequency of cyclones is enhanced in summer compared to winter; cf. Fig. 4 in Wernli and Schwierz 2006). In contrast, the recent climatology by Guan and Waliser (2015) uses a combination of relative and absolute criteria (IVT larger than the local 85th percentile in the considered season, and IVT larger than  $100 \text{ kg m}^{-1} \text{ s}^{-1}$ ) and, as a consequence, their frequencies are limited to a maximum of 15% and show less geographical and seasonal variability. Further research is required to better understand whether many summer ARs identified with the fixed-threshold approach are meaningful, or whether seasonally varying selection criteria are essential when identifying ARs year-round.

- Generally, the spatial overlap of objectively identified TME, AR, and WCB features is rather limited. Most grid points that belong to one of the three features do not meet the criteria of the other features. This is an important result, because it highlights the difference of the three concepts and, therefore, justifies a separate treatment of these three concepts. The most frequent overlap occurs between TMEs and ARs, i.e., between the two features

that highlight regions of strong horizontal moisture transport. That TMEs and ARs do not agree more closely is mainly because most ARs do not originate in the tropics. There is little overlap of these features with WCBs, reflecting the strong contrast between horizontal moisture transport (TMEs and ARs) and vertical ascent of moist air masses (WCBs), which usually reduces the former because of precipitation.

Together, these findings clearly show that TMEs, ARs, and WCBs are related but by no means identical concepts of atmospheric flow. They focus on different aspects of moisture transport and must not be used as synonyms. In particular, the strong ascent in WCBs and the associated condensation and rain-out are detrimental to the strong horizontal moisture transport required for ARs, and, therefore, WCBs limit the meridional extension of ARs. ARs most likely occur in regions with weak baroclinicity and weak large-scale ascent (where strong horizontal moisture transport can easily occur), in contrast to WCBs, which require strong baroclinicity, i.e., strongly sloping isentropic surfaces, because of their strong ascent. In some cases, however, WCBs and ARs overlap almost perfectly (e.g., Fig. 2.5a), pointing to a balance between rain-out because of ascent in a WCB and strong surface evaporation and low-level moisture convergence. Next, Sect. 2.4 discusses the detailed moisture budget along ARs, and then Sect. 2.5 summarizes basic dynamical aspects of the generation and depletion of IWV along ARs. The large case-to-case variability must be highlighted: individual cyclones can be associated with strongly different patterns of TMEs, ARs, and WCBs, and this pattern can change along the life cycle of a cyclone (as shown in Fig. 2.5). Therefore, no prototype configuration of the three features fits most situations.

**Fig. 2.8** Schematic of a TME–AR–WCB configuration related to an extratropical cyclone (label “L”). Parts of the AR overlap with TME trajectories, and others with WCB trajectories. The main ascent phase of the WCB does not overlap with the AR, because of strong condensation and rain-out. Such a configuration is observed (e.g., Fig. 2.12) but should not be regarded as representative of all ARs and/or extratropical cyclones



That said, Fig. 2.8 illustrates a schematic depiction of a specific flow configuration that shows a common interaction. In the equatorward part of the AR, partial overlap with a TME occurs. Further poleward partial overlap of the AR with WCB occurs, but, as the WCB rises, its moisture is strongly reduced because of rain-out and, therefore, most parts do not fulfill the AR criteria. Note that, consistent with the climatological results presented in this section, this situation does not include areas where all three phenomena coincide.

Finally, the presented climatologies and feature overlap values are, of course, quantitatively sensitive to the specific thresholds used to define the features. However, the main conclusions related to the different seasonality, geographical pattern, and the limited overlap of the features likely remain valid for moderate modifications of thresholds. The results contribute to a comprehensive portrayal of the fascinating complexity of the atmosphere’s water cycle and, ideally, will stimulate further research into TMEs, ARs, and WCBs.

## 2.4 Water Vapor Transport in ARs

The term “atmospheric river” creates powerful associations: imagine a stream of water (vapor) in the atmosphere that matches in volume the Earth’s largest actual rivers on land (Sect. 2.2). ARs are most frequent over ocean areas, where moisture is abundant; cyclones can intensify substantially because of the lower surface friction over water than over land, and thus can form extensive frontal structures. When the air masses that carry these massive vapor masses are forced upward (e.g., by topography as ARs make landfall, or

when transitioning to a WCB, see Sect. 2.5), they cool, and the water vapor condenses and precipitates. Precipitation can sometimes persist for extended periods in one region, which can cause enormous disasters, such as flash floods and landslides (see Chap. 5, “Effects of ARs”). A question that needs to be answered to understand the causes of such hydrological extremes is, therefore, how water is transported in an AR. In addition, understanding where the moisture sources are located could provide insight into what controls AR intensity.

The moisture contained and transported within ARs is their defining characteristic. Images of IWV and IVT sometimes show ARs as narrow filaments that extend from a tropical reservoir of high IWV (Sect. 2.2). This spatial connection suggests the tropics as the principal source of the water vapor transported poleward within ARs. Using different methods, several studies of the air mass and moisture transport within ARs have shown that the true picture is more complex (Bao et al. 2006; Ralph et al. 2011; Sodemann and Stohl 2013; Cordeira et al. 2013). In particular, these studies indicate that although some tropical water vapor may indeed reach higher latitudes within ARs, the bulk of the transported moisture originates from large-scale horizontal moisture convergence in the subtropics and mid-latitudes (Sect. 2.3), implying shorter average transport distances of the water vapor than the AR length. Unlike the “channel flow” perspective suggested in a vertically integrated view, ARs are time-evolving, dynamic, three-dimensional (3-D) features embedded in the large-scale atmospheric flow (Sect. 2.5). Considering all dimensions naturally adds complexity to understanding AR moisture transport.

This section summarizes the current state of knowledge on how moisture is transported within ARs, including where moisture sources are located, and how they are connected to the formation, maintenance, and shape of ARs, and to their decay. The moisture budget of ARs and its changes during their life cycle are considered first. Next, the spatial dimensions of how water vapor is transported horizontally and vertically within ARs are explored. A discussion follows of the advantages and drawbacks of different available methods from which these results were obtained. This section concludes with how moisture transport in ARs could affect dynamical processes, and research areas where knowledge on AR moisture transport should advance.

### 2.4.1 Moisture Budget During the AR Life Cycle

An AR life cycle can be divided into three stages: development, evolution, and decay (Cordeira et al. 2013). During an AR's life cycle, moisture continuously enters and leaves the moisture band that constitutes the AR. Moisture is added to an AR by processes such as southerly inflow, lateral convergence, and surface evaporation. Moisture is removed by precipitation, outflow, and moisture divergence. So far, the various contributions of these terms in their entire life cycle to the moisture budget of an AR have been only partly evaluated.

The traditional analysis of an AR's moisture budget often focuses on the mature stage of its life cycle. Maps of IWV and IVT typically suggest a connection between a tropical reservoir and a landfall region in the extratropics (Zhu and Newell 1998). Early studies of ARs noted their close relationship with cyclones and their life cycles (Newell et al. 1992). These studies also found that there appears to be a relationship between ARs and explosive cyclones ("bombs") (Zhu and Newell 1994), and that tropical cyclones can induce a strong poleward transport of tropical moisture that feeds into ARs (Stohl et al. 2008). While that instantaneous perspective allowed the transient nature of these phenomena and their association with specific synoptic patterns to be identified, only limited insight was gained into moisture sources and the actual moisture transport in ARs. This has probably led to the misleading perception that the moisture is sourced upwind of the AR's entrance region, transported in the atmosphere all the way along the AR, and lost where the AR terminates. In reality, the picture is more complicated, because an AR is not a static feature that "hoses" water from a reservoir to a target area. ARs evolve over time and change both their shape and position. Furthermore, a vertically integrated perspective masks the fact that air masses ascend as they move poleward, water condenses, and thus moisture is

replenished rather than materially conserved during poleward transport.

Following the air masses of precipitation extremes backward in time to their origin provides insight into the leading transport processes. Using trajectory analyses, Bao et al. (2006) found that although poleward transport of tropical moisture may occur along an IWV band (i.e., an AR), in many cases, local moisture convergence is primarily responsible for forming the bands of enhanced IWV. For the case of an AR making landfall on the US West Coast during 1–5 January 1997, 4-day backward trajectories released in the region of high IWV show air mass origins that cover a wide range of latitudes of 10–40°N (Fig. 2.9a). In addition, moisture continuously converges laterally into the AR along the cold front (Fig. 2.9b, contours). The convergence enhances the IWV anomaly and replenishes moisture lost by precipitation. Without that replenishment, the IWV anomaly of an AR would be dissipated quickly. A climatological study by Ryoo et al. (2015) confirmed that these characteristics are indeed typical for ARs.

Considering trajectories alone indicates air flow, but does not delineate the moisture's evaporation sources. The spatial extent of an AR's moisture sources becomes apparent when Lagrangian moisture source diagnostics are applied on the backward trajectories (see Sect. 2.4.3 for details). Using such a diagnostic on backward trajectories, the source regions of moisture for a precipitation extreme in western Norway from an AR were shown to cover vast areas of the North Atlantic (Fig. 2.10a). Moisture converged from both north and south of the AR, supplemented by transport of moisture from the subtropics within two former hurricanes, more than a week before the AR impinged on the Norwegian coast at 60°N (Stohl et al. 2008). Such Lagrangian backward tracing of air masses is the basis for several methods that can be used to identify AR moisture sources. The analysis in Fig. 2.10a identifies where either evaporation or precipitation dominated within air masses along the 12-day transport path toward the target region in western Norway. A detailed accounting of increases and decreases of moisture in air parcels that move along the trajectories enables a clearer delineation of how convergence and the tropics contribute to the final target region (Fig. 2.10b). In combination, both methods show a large footprint of the AR moisture sources and underline the role of both local convergence and long-range transport in an AR's moisture budget (again, see Sect. 2.4.3).

A less well-established part of an AR's moisture budget concerns the evaporation within the AR band itself from the underlying surface. Observations of evaporation during cold-frontal passages over the ocean show that, despite high wind speeds, evaporation is small within the warm sector, ahead of the cold front (Persson et al. 2005). The reason is that air

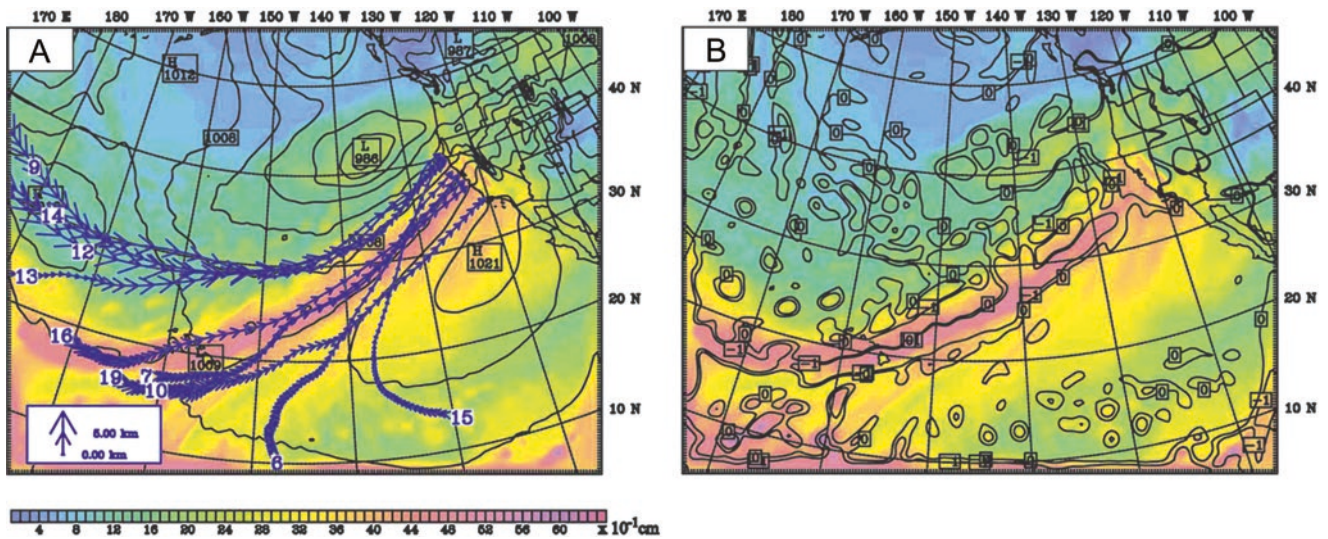


**Fig. 2.9** Air mass trajectories (*thick black lines*) calculated for 96 h backward for an AR making landfall at the US West Coast. *Contours* in (a) are sea-level pressure (hPa), and contours in (b) are convergence at 0 and  $-1.0 \times 10^{-5} \text{ s}^{-1}$ . (Bao et al. 2006, Fig. 7b, c)

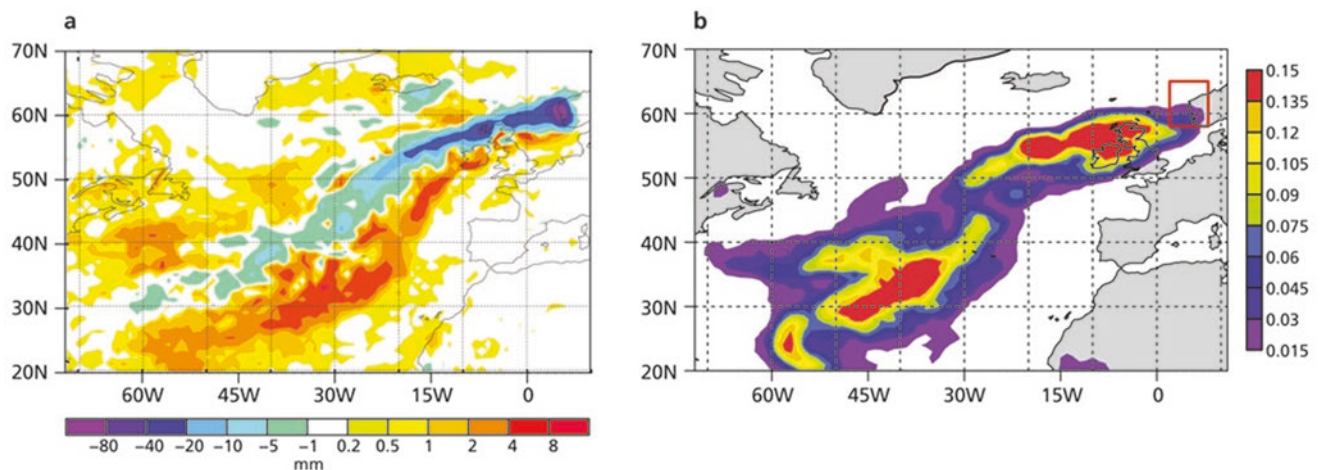


**Fig. 2.10** (a) Time-integrated Lagrangian  $e - p$  (evaporation minus precipitation; mm) budget over 12 days before arrival of intense precipitation at the west coast of Norway during a landfalling AR on 13–14 September 2005. Negative values indicate that precipitation dominates moisture removal from the air mass; positive values indicate net evaporation into air masses on the way to the target area (2–8°E and 58–65°N)

for the same period in southern Norway. Note the asymmetric color scale. (Stohl et al. 2008, Figure 9d). (b) Moisture sources for precipitation in the target area (*red box*) identified from the Lagrangian moisture accounting method of Sodemann et al. (2008a). Units in (b) are  $\text{kg m}^{-2} \text{ day}^{-1}$  of evaporation contributing to precipitation in the target area

masses advected in the warm sector are relatively moist, maybe close to saturation, and therefore do not lead to substantial evaporation from the surface. Thus, within an AR characterized by poleward advection of moist air, evaporative contributions from the underlying surface may also be expected to be negligible. On the other hand, evaporation from falling hydrometeors may also moisten the lower troposphere and thus reduce the moisture loss within the

AR. Further studies on these aspects of the AR moisture budget are clearly needed.

In summary, horizontal convergence in the extratropics and long-range transport from subtropical and tropical areas appear to make relevant contributions to the moisture budget of an AR. The joint role of these source processes during the life cycle of an AR is exemplified in Fig. 2.11. In a case study of two intense AR events in October 2010, tropical source

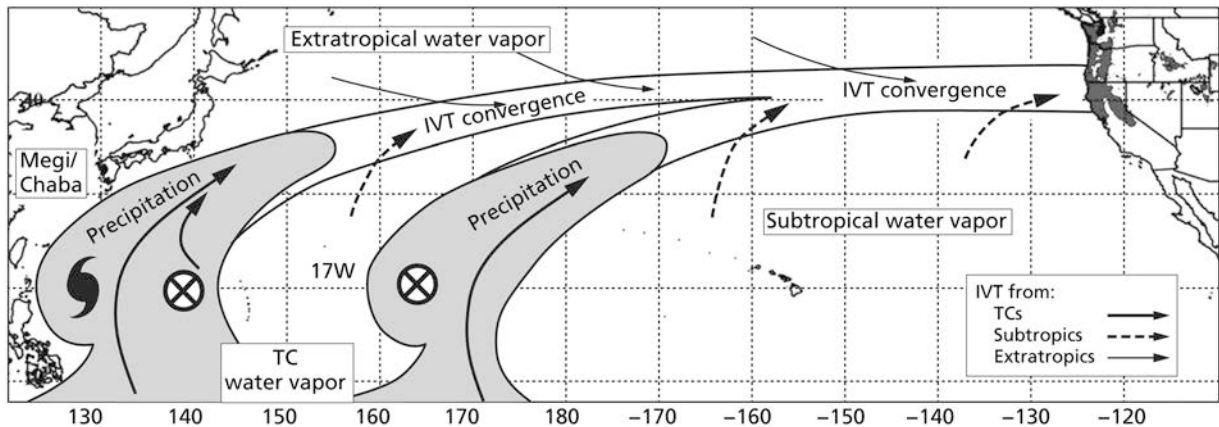


**Fig. 2.11** Schematic overview of water vapor source regions during AR development (i.e., tropical source regions) and during AR evolution (i.e., subtropical and extratropical source regions) of two ARs making landfall in October 2010 in the western USA. The 48-h accumulated

precipitation ending at 1200 UTC 25 Oct 2010 is contoured and shaded in gray above 50 mm. Thick solid, dashed, and thin solid arrows denote moisture contributed by tropical, subtropical, and extratropical regions at different stages of the AR life cycle. (Cordeira et al. 2013, Fig. 11e)

regions related to former tropical cyclones were more influential during the development phase. Subtropical and extratropical contributions took over during the later AR evolution phase, as indicated by the solid and dashed arrows in Fig. 2.11.

Toward the end of an AR's life cycle, moisture-removal processes become increasingly important. Eckhardt et al. (2004) highlighted the co-occurrence of ARs and the so-called WCB of extratropical cyclones. WCBs source their moisture in the warm sector of the cyclone, and sometimes within ARs (Sect. 2.3). A key characteristic for separating ARs and WCBs is that the first are defined by high water vapor transport, whereas the latter are characterized by rapid and strong ascent, leading to condensation, deep cloud formation, and precipitation (Sects. 2.3 and 2.5). This is illustrated by comparing an infrared (IR) satellite image and a picture of IWV for the same AR event and at the same time. Where the IWV imagery shows the familiar AR signature of an elongated extension of high IWV from a subtropical reservoir to mid-latitudes (Fig. 2.12b), the IR image shows no or mostly warm low-level clouds in the southwestern part of the AR (Fig. 2.12d), as indicated by the dark blue colors. This is a region with little vertical motion. As the AR transitions into the WCB further to the northeast, vertical motion increases and more widespread cloud formation sets in, eventually forming the broad band of intense, high-reaching clouds typical of a WCB (Fig. 2.12d, red areas near the UK). Note that removal of moisture from precipitation along the way is also expected within the area of the AR that is dominated by shallow clouds. Such removal along the way has not yet been quantified in detail.

## 2.4.2 Horizontal and Vertical Moisture Transport and AR Maintenance

AR bands can extend over thousands of kilometers (Ralph et al. 2004). This can be identified from IWV or IVT that exceed some threshold value (Sect. 2.2). However, as just discussed in Sect. 2.4.1, most of the moisture is not transported along the whole AR. Rather, moisture convergence along the AR continuously replenishes moisture lost by precipitation within the AR itself. The distance over which moisture is actually transported seems to depend primarily on the size of the cyclone with which the AR is associated. Examples shown in Dacre et al. (2015) suggest that in smaller cyclones at the poleward or downstream end of the North Atlantic storm track, AR moisture is mainly of local origin. However, ARs associated with deep and large troughs can indeed transport moisture over thousands of kilometers, including northward transport by about 20° of latitude and more (Bonne et al. 2015).

Sodemann and Stohl (2013) found that ARs can also be associated with more than one cyclone. This requires that a pronounced wave pattern is present in the upper troposphere, resembling an anticyclonic life cycle (a so-called LC1; see Sect. 2.4 and Fig. 2.15) in Thorncroft et al.'s (1993) cyclone life cycle classification. At the western edge of the AR, small cyclones can develop from frontal waves. The cold fronts of these small cyclones add moisture to the AR by convergence with their warm-sector air masses ahead, while their WCB air stream taps the moisture from the AR. Thus, such frontal wave cyclones each contribute moisture to the AR at one end, and feed on it for their spin-up and development at the other. Subsequent cyclones thus profit from the moisture

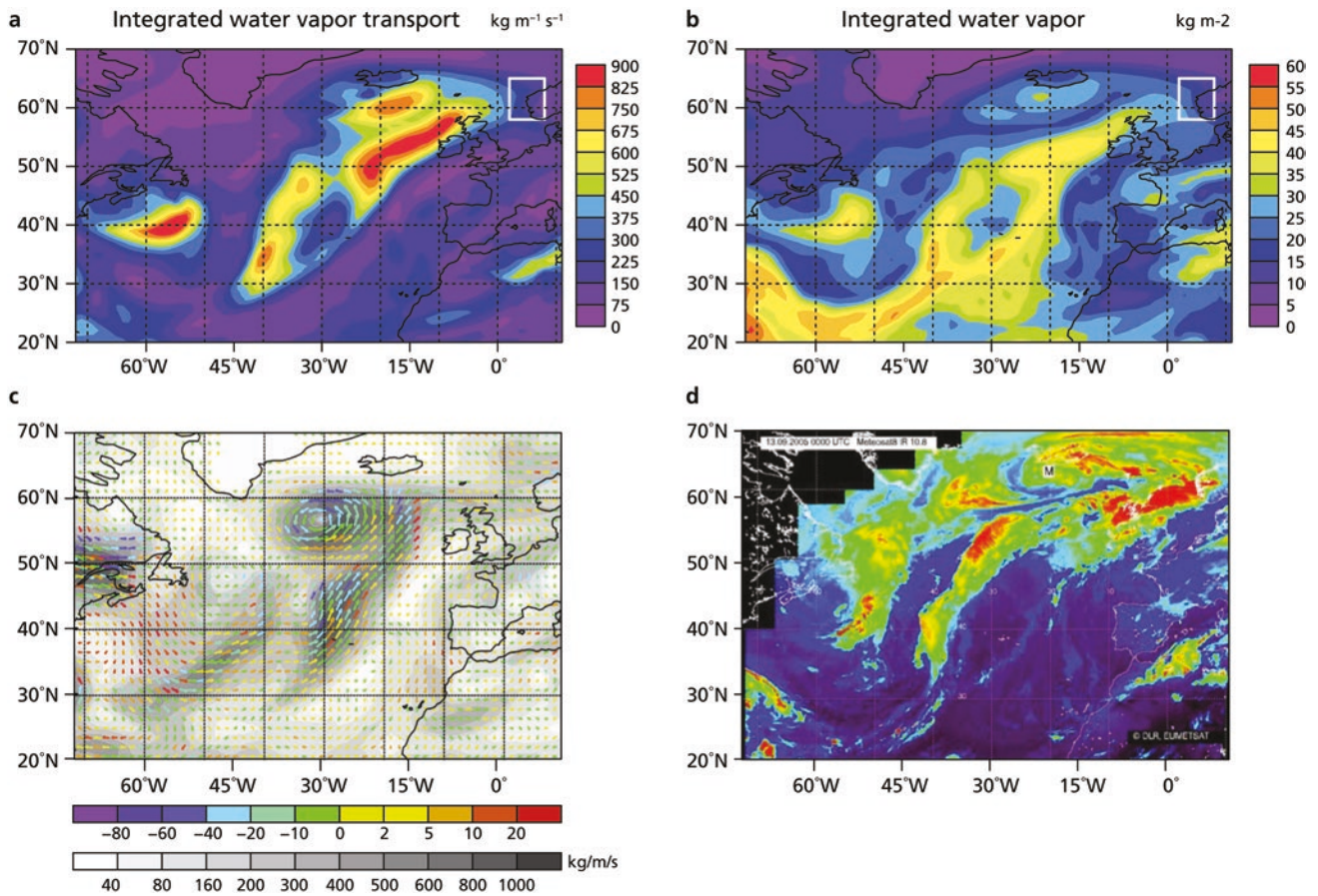


**Fig. 2.12** Case study of an AR event that caused flooding on the western coast of Norway during 13–14 Sep 2005. The panels show (a) integrated vapor transport (IVT,  $\text{kg m}^{-1} \text{s}^{-1}$ ) and (b) integrated water vapor (IWV,  $\text{kg m}^{-2}$ ) at 00 UTC on 13 Sep 2005 from European Centre for Medium-Range Weather Forecasts (ECMWF) ERA-Interim reanalyses, (c) vertically integrated water vapor transport (arrows) and surface

freshwater flux (shading,  $\text{kg m}^{-1} \text{s}^{-1}$ ) at 00 UTC 12 Sep 2005 from ECMWF analyses, (d) Meteosat-8 infrared brightness temperatures in 10.8 m channel at 00 UTC on 13 Sep 2005. Red colors indicate high (cool) cloud-top temperatures. (Panels (c, d) from Stohl et al. 2008, Figs. 6c and 4a)

transported poleward by previous cyclones, leading to a “hand-over” of moisture between subsequent short-lived cyclones (Sodemann and Stohl 2013; see also Fig. 2.13). According to this picture, ARs can be longer-lived than the individual cyclones. Following Dacre et al. (2015), the AR can therefore be considered as the footprint which a decaying cyclone leaves behind on its way toward higher latitudes. Although detailed studies do not exist on how a moisture “hand-over” process between cyclones influences the moisture sources that contribute to the AR, it is clear that the warm sectors of the individual cyclones each contribute moisture to the AR, thus generating a large and complex source region for the moisture present in the AR. It is also evident that the moisture source regions will be very different for different stages of the AR evolution, with lower-latitude source regions being initially most important, but with higher-latitude sources becoming more important with time (as just discussed in Sect. 2.4.1). Yet, although the moisture of low-latitude origin may diminish as the AR reaches

higher latitudes, it may be important for spawning daughter cyclones and thereby prolonging the AR’s development. Furthermore, even small amounts of low-latitude moisture can be important for extreme events at high latitudes, because they might cause critical precipitation thresholds for flooding to be exceeded.

Another aspect of ARs is their 3-D structure. Although most moisture is concentrated in the lower troposphere (Ralph et al. 2004), the upper troposphere can guide their formation dynamically (Sodemann and Stohl 2013; Cordeira et al. 2013), and, at later development stages, AR air masses can rise into the upper troposphere within the WCB (Eckhardt et al. 2004). Thereby, the moisture source regions are also very different for different altitudes. As air masses ascend in a (moist) isentropic fashion in a WCB, a vertical cross-section through an AR shows moisture that originates from lower-latitude sources stacked over moisture that originates from higher latitudes (Fig. 2.14a, d). Thus, at low altitudes, moisture is expected to be mainly of local origin, whereas at

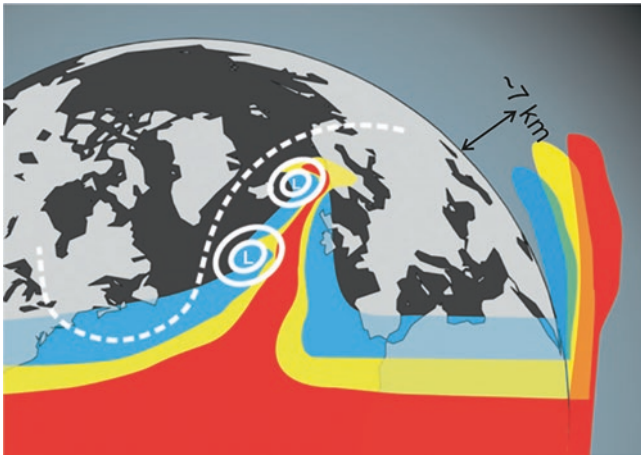


**Fig. 2.13** Schematic view of the moisture transport during anticyclonic (LC1-like) wave breaking with a meridional upper-level jet. *Dashed white line* shows the orientation of the upper-level jet, *solid white lines* show sea-level pressure (SLP), and *shaded colors* indicate oceanic moisture from source regions at different latitudes (*red* most southerly, *blue* most northerly). The right-hand side of the figure shows a vertical cross-section of moisture originating from different altitudes lifted to different altitudes. (Sodemann and Stohl 2013, Fig. 10a)

higher altitudes, moisture arrives from distant sources, as also shown schematically in Fig. 2.13 (right margin). Even though this elevated moisture of distant origin contributes relatively little to the total IWV, it could be responsible for precipitation enhancement over topography according to the seeder–feeder mechanism (Dacre et al. 2015), and high-altitude latent heat release is also important for the dynamics of cyclone evolution, and for atmospheric stability.

One feature that complicates the analysis of water source regions is the evaporation of falling precipitation below the cloud base, as evidenced by stable water isotope studies (Yoshimura et al. 2010). Thus, trajectory studies of the origin of water vapor in the lower troposphere may not always correctly identify the source region of the water vapor itself, which may be found at lower latitudes (i.e., typical of higher-altitude moisture sources) than the trajectories indicate. The future potential of stable isotopes to study processes and moisture sources that contribute to an AR is discussed further in Sect. 2.4.4.

### 2.4.3 Methods for Obtaining an AR Water Budget

Which methodology is used to trace and identify AR water budgets turns out to be central to the information obtained on moisture transport in ARs. The initial, most straightforward approach to quantify moisture transport in ARs was to consider time-averages or snapshots of the vertically integrated Eulerian IVT (Fig. 2.12a). When displayed as vectors, as in

the original work by Newell et al. (1992), implicit streamlines of the IVT seem to indicate source regions in the tropics (Fig. 2.12c). As discussed above, however, this perspective is misleading because ARs are 3-D, time-evolving, dynamical features with a complex moisture budget, and their moisture sources and sinks are not faithfully represented by static snapshots of vertical moisture integrals (see Sects. 2.2 and 2.5).

The time-evolving nature of ARs substantially complicates budget studies. For example, evaluating Eulerian moisture budgets from inflow, outflow, evaporation, and precipitation within ARs requires a calculation domain that adjusts to the shape and position of the evolving AR feature. Lagrangian forward and backward trajectories provide an intuitive perspective that follows the flow. However, trajectories “belonging” to the AR must first be identified. Air-parcel trajectories have been used in several studies to investigate the air-mass transport within ARs. Bao et al. (2006) and Ryoo et al. (2015), for example, investigated the air-mass transport with 2- to 4-day backward trajectories for different landfalling ARs, and inferred the moisture origin from the transport path of the air masses. Cordeira et al. (2013) traced quantities such as water vapor mixing ratio along 3-day forward and backward trajectories over the Pacific that indicated moisture uptake and loss during the air-mass transport. The specific humidity budget along trajectories has been used in many studies to reveal information about sources and sinks of water vapor during transport (Stohl and James 2004; Stohl et al. 2008). When such a Lagrangian  $e - p$  (evaporation minus precipitation) diagnostic is combined with a weighting algorithm that takes care of moisture lost from or added to an air parcel over several days, spatial maps can be obtained of the evaporative moisture sources of either precipitation events or water vapor in an air mass (Sodemann et al. 2008a; Bonne et al. 2015). Figure 2.10b shows the moisture sources of the AR event from 13–14 Sep 2005 using the quantitative moisture source diagnostic of Sodemann et al. (2008a), with the data set of Läderach and Sodemann (2016) based on the ECMWF’s ERA-Interim reanalysis data. The moisture source map can be interpreted as part of total evaporation that contributes to precipitation falling in the target domain at the west coast of Norway (2–5°E, 58–65°N). The moisture sources cover a wide area and extend into the subtropical North Atlantic. In comparison to the  $e - p$  map (Fig. 2.10a), more local sources are identified in the moisture accounting map (Fig. 2.10b). These local sources appear to have been masked by rain-out of air masses on the way toward the target area in the  $e - p$  map.

Both trajectory-based methods, however, have common and individual limitations. An important limitation of common off-line calculation of Lagrangian trajectories is the temporal and spatial interpolation of the meteorological fields done during trajectory calculations. In particular, in the

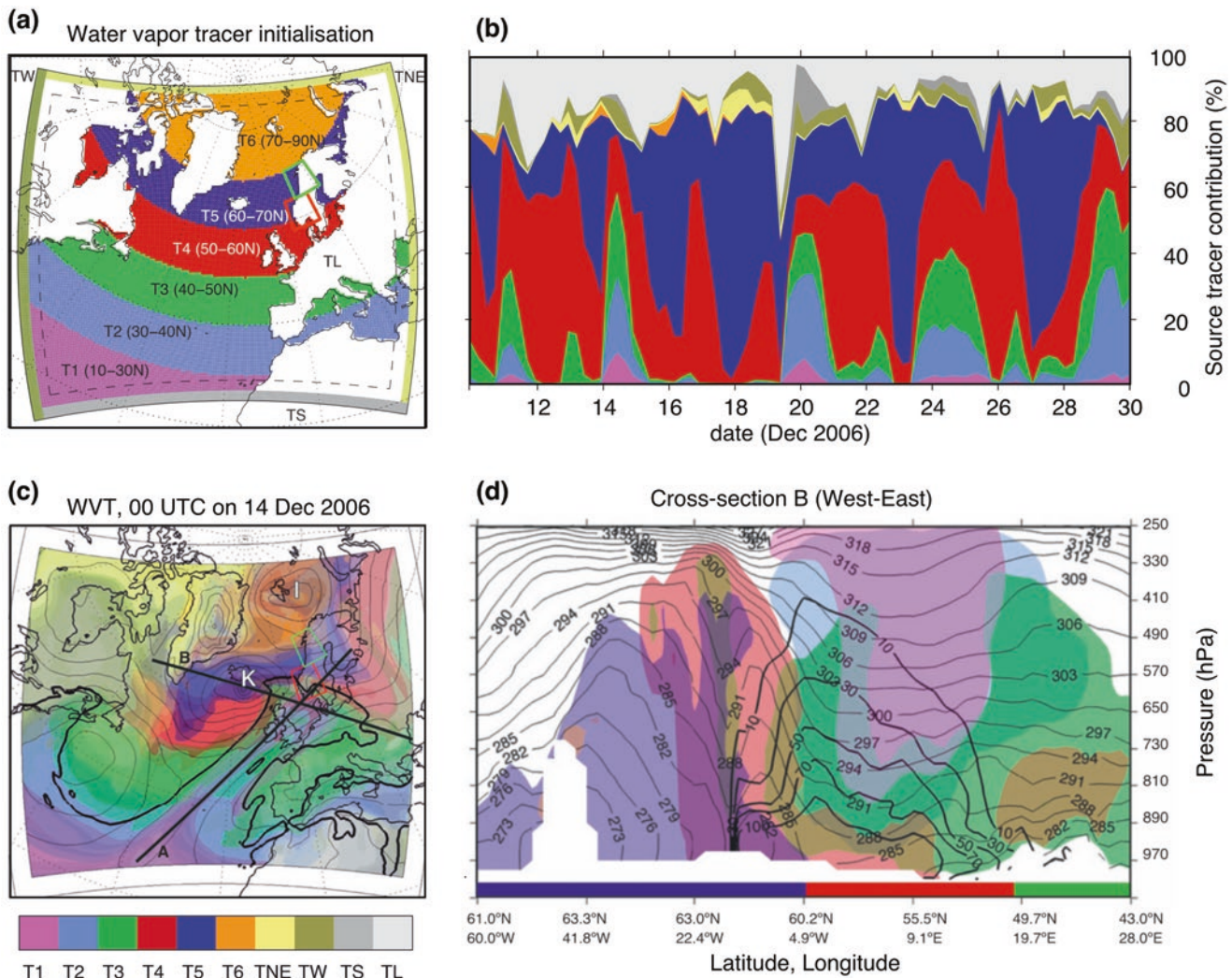


**Fig. 2.14** (a) Initial water tracer evaporation source regions in a regional model simulation with latitude band initialization. (b) Time-series of Eulerian water-vapor tracer contributions over southern Norway (red box in Panel a). (c) Snapshot of water-vapor tracers during an AR making landfall in Dec 2006. Colors show contributions from

moisture with sources at different latitudes to IWV. Black contour at 14 mm IWV outlines AR region. (d) Vertical cross-section in West-East direction (letter *b* in panel c) of tracer fraction >30% of specific humidity (shading) and meridional moisture flux (black contours)

light of continuously increasing spatial resolution of the wind field data, it is important to increase the temporal resolution of input fields as well (Bowman et al. 2013). One promising solution to such aspects of the temporal and spatial interpolation during off-line calculations may be on-line trajectory calculations (Miltenberger et al. 2013), but they have not been applied in this context so far. Because the origin of water vapor is not easily derived from common water-vapor measurements, new observational approaches are needed. In particular, the inclusion of stable water isotopes in AR field measurements could help to constrain the contribution of different moisture sources to their budget (Coplen et al. 2008; Yoshimura et al. 2010).

A second, alternative on-line calculation method to study moisture sources and transport in atmospheric models are computational water-vapor tracers. Implemented as a sec-

ondary hydrological cycle in a model, the water tracers passively take part in all resolved and parameterized processes that affect the model's water vapor (Sodemann and Stohl 2013). In other words, water released from a specific oceanic source region can be tagged with a "color" tag, evaporated from the surface, and then be traced as water vapor of the same color through the atmosphere (see Fig. 2.13). Tracer water released from different pre-defined source regions—for example, from specific latitude bands in the North Atlantic Ocean—can be tagged with different colors, which provides detailed insight into the vertical and horizontal collocation of moisture that evaporates from different regions and time-periods (Fig. 2.14a, c). The tagged water vapor will also produce precipitation with the same color tag. For a winter season with frequent AR events in southern Norway, the water-tracer method allowed the different source contri-

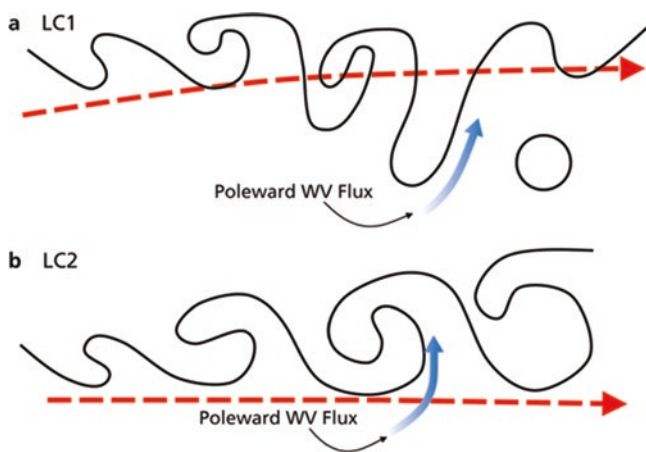


**Fig. 2.15** Schematic representations of mid-latitude storm track evolution typifying (a) an LC1-type (anticyclonic wave breaking) life cycle and (b) an LC2-type (cyclone wave breaking) life cycle. The *black contour* represents a characteristic potential temperature contour on the 2-potential vorticity unit (PVU) surface. The *dashed black line* identifies the approximate position of the mean jet stream axis at each stage. The *gray-to-black arrow* indicates the potential region of poleward water vapor (WV) flux. (Adapted from Thorncroft et al. 1993)

butions for each event to be quantified (Fig. 2.14b). As ARs impinge on the target domain (Fig. 2.14a, red box), the contributions of southerly tracers to precipitation in the area increase, as shown by the spikes in green, light blue, and purple tracers, at the expense of local tracers, colored dark red and dark blue (Fig. 2.14b). On average, during the studied period, remote sources contributed only about one-third of the total rainfall (Sodemann and Stohl 2013). Although achieving budget studies for fixed target domains is straightforward, considering the budget of ARs again requires adoption of a budget calculation that moves with the AR during its life cycle.

It is important, thereby, to point out that both Lagrangian and Eulerian tracer methods, at least to first order, provide consistent results. Although the contribution of remote water vapor is generally larger for the Lagrangian approach, both methods show a consistent general pattern of a blend of southerly moisture sources that have converged horizontally within the AR zone. This information can be obtained explicitly from the Lagrangian moisture diagnostic as a quantitative map of moisture source contributions that shows the evaporation sources during the study period as a meridionally-extending core zone that is supplemented by moisture supplied from the entire North Atlantic Ocean basin. Ultimately, Eulerian and Lagrangian methods are complementary and can work hand-in-hand to provide a comprehensive view of the moisture cycle in ARs: The water-vapor tracers show the entire moisture-transport process of the AR and the surrounding atmosphere; the Lagrangian method provides a detailed mapping of the moisture source regions.

#### 2.4.4 Conclusions, Implications, and Future Directions

Moisture transport within ARs is clearly more complex than suggested from 2-D, vertically integrated snapshots of water vapor and water vapor transport. During the entire life cycle of an AR, moisture converges horizontally into ARs before being transported poleward, ascending, partially condensing, and, finally, precipitating. The moisture delivered by ARs as they make landfall is, therefore, an intricate vertically and horizontally variable combination of water from different source regions. Quantitative model studies are still very limited, both in the Eulerian and Lagrangian model frameworks. The available studies commonly suggest that although long-range moisture transport from the tropics is important for ARs making landfall at rather low latitudes (e.g., in California), it is the exception rather than the rule for ARs impinging on higher-latitude regions (e.g., Northern Europe). More quantitative studies in other regions are clearly needed to more firmly establish the AR moisture budget. These should also include the role of surface evaporation within the AR.

Knowledge about AR moisture transport—and the moisture source regions—has important implications for atmospheric energy transport and radiative effects. Condensational latent heat release couples oceanic sources to far-away atmospheric regions, transferring energy meridionally and vertically. Injecting high amounts of water vapor in a cold and dry polar environment substantially affects the atmosphere's radiative budget. Cloud formation from this water vapor is a further aspect of significance for the climate system. Such aspects of ARs have, so far, received little attention (with the exception of Woods et al. 2013 and related work). Clearly, in the framework of a changing climate, the connection between moisture transport in ARs and energy transfer to high latitudes calls for further analysis.

So far, several conclusions in this chapter are based on only a few or even individual case studies. In addition, current analyses are predominantly based on an atmospheric model's representation of reality, rather than direct observations. The currently used numerical methods are powerful tools for further investigations of how ARs modulate meridional water vapor transport. Eulerian and Lagrangian methods can thereby be seen as complementary. At the same time, model studies can benefit from further improvements such as on-line trajectory calculations for the Lagrangian approach (Miltenberger et al. 2013) or cloud-resolving modeling for Eulerian water-vapor tagging to reduce the uncertainty in model simulations (Winschall et al. 2014).

To more closely tie the water-vapor transport as simulated by atmospheric models to reality, an observational tracer of water-vapor origin and transport would be required. Stable water isotopes are potentially such a tool, because they inte-

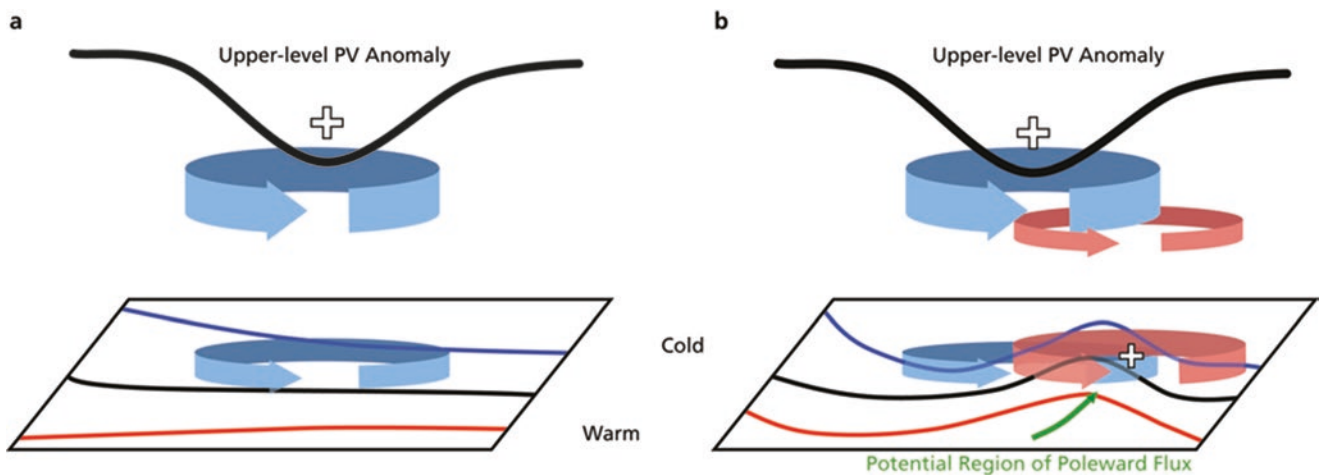


**Fig. 2.16** A schematic representation of cyclogenesis with the approach of an upper-level PV anomaly over a low-level baroclinic zone. In (a) the cyclonic circulation associated with the upper-level PV anomaly (indicated by blue upper-level arrow around the “+” symbol) induces a weak cyclonic circulation (given by arrow thickness) to the near surface. The sense of the low-level cyclonic circulation will induce temperature advectations ahead of and behind the upper-level PV anomaly. In (b) the warm temperature anomaly

that has developed can be represented by a low-level positive PV anomaly (represented by the low-level “+”). The cyclonic circulation associated with the low-level PV anomaly will induce a weak upper-level cyclonic circulation, given by the red arrows, thus reinforcing the upper-level PV anomaly and slowing down its eastward progression. The green arrow indicates a potential region of poleward water vapor (WV) flux. (Adapted from Hoskins et al. 1985)

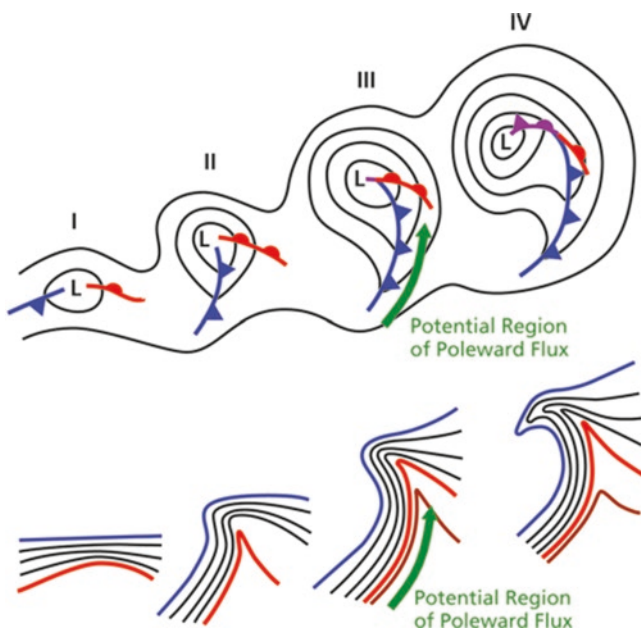


**Fig. 2.17** Conceptual model for cyclone evolution following the Norwegian cyclone model that shows idealized lower-tropospheric geopotential height and fronts in the top panel and lower-tropospheric potential temperature in the bottom panel. The green arrow indicates a potential region of poleward water vapor flux. (Adapted [colorized] from Schultz et al. (1998) and based on Bjerknes and Solberg (1922))

grate the entire atmospheric transport history during phase changes from source to sink (e.g., Jouzel et al. 2013; Sodemann et al. 2008b). So far, this information has been

used in only a few AR case studies (Coplen et al. 2008, 2015; Yoshimura et al. 2010; Bonne et al. 2015). Future field campaigns will, ideally, be able to cover the large spatial extent of moisture sources during AR events, including tracers of moisture origin, such as stable isotopes. This can provide the information necessary to tie model simulations to reality for the location of moisture sources, the spatial extent and duration of moisture transport, and the contribution of different components to the AR moisture budget.

## 2.5 ARs and Extratropical Dynamics

The Earth’s atmosphere is a fluid that primarily comprises dry air with comparatively small concentrations of water vapor. This atmospheric fluid is bound to Earth via gravity and is constrained by the laws of fluid dynamics that describe relationships among fluid velocity, pressure, density, and temperature. The atmosphere is in a perpetual state of motion from spatio-temporal variations in solar radiation on a rotating planet covered mostly in water. These combine to give rise to preferential regions of enhanced atmospheric water vapor concentrations and preferential flow patterns that can transport, aggregate, or deplete—because of cloud formation and precipitation—large quantities of atmospheric water vapor.

Atmospheric water vapor is produced within the hydrologic cycle in large quantities via evaporation of liquid water, sublimation of ice, and transpiration in vegetated areas,

among other less common processes. An estimated  $420 \times 10^3 \text{ km}^3$  of water vapor is added to the atmosphere via evaporation each year, whereas an additional  $70 \times 10^3 \text{ km}^3$  of water vapor is added to the atmosphere via transpiration each year (Anderson and Strahler 2008, p. 125). The amount of water vapor per unit mass of air is constrained by the relationship between partial pressure of water vapor and temperature. For example, the saturation [water] vapor pressure, or the partial pressure of water vapor at saturation, increases in a roughly exponential nature from  $\sim 6 \text{ hPa}$  at  $0^\circ\text{C}$  to  $\sim 16 \text{ hPa}$  at  $15^\circ\text{C}$  (see Fig. 4.8 of McElroy 2002, p. 38) following the closed form of the Clausius–Clapeyron equation (see Miller 2015 [Eq. 7.45]). A large majority of global atmospheric water vapor content is contained within the troposphere at higher barometric pressures (following from the relationship between temperature and pressure from the Ideal Gas Law) and at more tropical latitudes at warmer temperature (see Fig. 5.4 of Anderson and Strahler 2008). This relationship is readily observed via sub-daily Special Sensor Microwave Imager (SSM/I) satellite imagery of IWV (see Sect. 2.2), with the maximum in IWV content across the tropics in the so-called IWV reservoir and the minimum in IWV across polar regions.

Further analysis of the sub-daily global IWV from SSM/I satellite imagery highlights the filamentary structures of poleward extrusions of enhanced regions of IWV that have been defined in previous literature as tropospheric rivers (Newell et al. 1992) or in previous sections of this book as ARs. As shown in Sect. 2.2, these filamentary structures are found in the warm-sector region of cyclones ahead of surface cold fronts; herein, their existence is attributed to high-frequency synoptic-scale circulations embedded within the mid-latitude storm track and the development of mid-latitude cyclones. This Sect. 2.5 also investigates the high-frequency synoptic-scale processes that comprise the mid-latitude storm track and their relationship to ARs. Additional information on many of the mid-latitude cyclone dynamics discussed next in Sects. 2.5.1 and 2.5.2 is available in traditional synoptic-scale textbooks (e.g., Bluestein 1992; Carlson 1998; Holton 2004; Martin 2006, among others). See Lau et al. (2011) for a review of intra-seasonal variability in the atmosphere–ocean system that link weather and climate processes, and Newman et al. (2012) for a review of the relative contributions of synoptic- and low-frequency eddies to time-mean atmospheric moisture transport. The subsequent review provides evidence for the formation and presence of ARs in the warm sector of canonical mid-latitude cyclones; however, with notable case-to-case variability in cyclone structures (and their evolution), notable case-to-case variability also exists in the processes that lead to AR formation.

### 2.5.1 Mid-Latitude Storm Track and Cyclogenesis

The general circulation of the atmosphere is maintained through the generation and depletion of atmospheric available potential and kinetic energy (Lorenz 1955). The mid-latitude storm track is, consequently, the manifestation of the depletion of atmospheric available potential energy and the generation of atmospheric kinetic energy observed via the release of baroclinic and barotropic instability in conjunction with development of large-scale eddies across preferential regions of the globe. The synoptic-scale eddies comprising the mid-latitude storm track largely take on the form of two paradigms associated with baroclinic Rossby wave life cycle behavior (Fig. 2.15; Thorncroft et al. 1993). The two life cycles, identified as Life Cycle 1 (LC1) and Life Cycle 2 (LC2), apply to the development and advection of mid-latitude upper-tropospheric troughs and their upstream (or downstream) ridges. During LC1 (Fig. 2.15a), or “anticyclonic” wave breaking (AWB), troughs tend to tilt from southwest-to-northeast, and zonally contract as they propagate along an anticyclonic arc toward the equator. In contrast, during LC2 (Fig. 2.15b), or “cyclonic” wave breaking (CWB), troughs tend to tilt from southeast-to-northwest, and zonally expand as they propagate along a more cyclonic arc toward the pole. Rossby wave breaking (RWB) in the exit regions of mid-latitude jet streams, particularly associated with LC1 events, can result in penetration of mid-latitude troughs into subtropical latitudes (Webster and Holton 1982; Matthews and Kiladis 1999). Such low-latitude RWB events have been implicated in the development of tropical cloud plumes (e.g., McGuirk et al. 1987, 1988), enhanced convection downstream of the trough (e.g., Moore et al. 2010), and the initiation of poleward water vapor transport out of the tropics (Knippertz 2007) along possible ARs that follow a pathway similar to a TME (e.g., Knippertz and Wernli 2010; Knippertz et al. 2013; see Sects. 1.1.4 and 1.1.5, as well as Chaps. 5 and 7. Although water vapor transport is the signature of ARs in the lower troposphere, recent work suggests that RWB is a characteristic of ARs in the upper troposphere (Payne and Magnusdottir 2014).

The genesis of individual surface cyclones, and their circulations that are able to mobilize greater amounts of water vapor in the lower troposphere (e.g., Bao et al. 2006; Sodemann and Stohl 2013) in the above-mentioned LC paradigms, can be described to first order by quasi-geostrophic (QG) theory. The QG theory explains atmospheric momentum in conjunction with a balance between the Coriolis force and pressure gradient force (i.e., geostrophic balance), and any small displacements or accelerations away from geostrophy that inertia affords (Holton 2004). By definition, the geostrophic wind is non-divergent such that any divergence

is the result of fluid expansion (or contraction) generated by fluid acceleration that follows the ageostrophic wind. Furthermore, atmospheric layers bound by regions of divergence or convergence must contain vertical motion according to the QG continuity equation. Thus, the total horizontal wind,  $V$ , comprises both the geostrophic wind,  $V_g$ , and the ageostrophic wind,  $V_a$ , and vertical motion is driven by convergence or divergence of  $V_a$ . Following QG theory, cyclogenesis therefore relates to upper-tropospheric divergence downstream of an upper-tropospheric trough. This creates a region of enhanced tropospheric upward vertical motion and influences lower-tropospheric convergence and the generation of cyclonic vorticity (Sutcliffe 1939, 1947; Sutcliffe and Forsdyke 1950) in the vicinity of a lower-tropospheric thermal gradient. The aforementioned cyclogenesis process has been named “Type B” (Petterssen and Smebye 1971) or “Stream II” (Davies 1997) cyclogenesis and is the result of cyclonic vorticity advection by the geostrophic wind in the upper troposphere that over-spreads an area of geostrophic warm air advection in the lower troposphere, or simply cyclonic vorticity advection by the thermal wind (Trenberth 1978).

An alternative way to visualize the cyclogenesis processes is through “potential vorticity (PV) thinking,” detailed in Hoskins et al. (1985). For adiabatic and frictionless flow, PV, as defined by Ertel (1942), is the product of earth’s vorticity and the static stability for a given isentropic surface. Maxima in tropospheric PV are typically found near the poles, where strong static stability and high absolute vorticity exist from the poleward increase of the Coriolis parameter. PV maxima extend equatorward from higher latitudes in the presence of strong static stability and troughs in the geopotential height field known as PV streamers (Appenzeller and Davies 1992), whereas minima in PV extend poleward from lower latitudes and are associated with weak static stability and ridges in the geopotential height field.

Figure 2.16 illustrates how an upper-tropospheric region of enhanced PV (e.g., a positive PV anomaly or PV streamer) can induce extratropical cyclogenesis: a positive PV anomaly will induce a cyclonic circulation through its Rossby penetration depth that extends to the near surface. Note that the southerly flow on the east side of the cyclonic circulation may support poleward water vapor flux and AR formation if proximate to the IWV reservoir (AR formation may also occur separate from the IWV reservoir; see Sect. 2.5.2). If the underlying surface is characterized by lower-tropospheric baroclinicity, the cyclonic circulation will also support the formation of a warm temperature anomaly at the surface downstream of the upper-tropospheric PV anomaly. The warm temperature anomaly is, consequently, also a lower-tropospheric positive PV anomaly and will, in turn, act to induce its own cyclonic circulation aloft. A positive feedback mechanism is established as the modified upper-tropospheric

circulation advects enhanced PV air aloft equatorward and, by the same circulation, advects weak PV air aloft poleward, which reinforces the pre-existing upper-tropospheric PV anomaly. According to QG theory, the requirements for cyclogenesis and cyclone intensification are also met with an upshear-tilted disturbance, which ensures maximum cyclonic (or potential) vorticity advection by the thermal wind over the surface cyclone (Martin 2006).

The above-mentioned storm track dynamics related to RWB and QG/PV frameworks for cyclogenesis provide evidence for synoptic-scale processes that may influence the poleward transport of water vapor from the IWV reservoir into mid-latitudes in association with RWB. These synoptic-scale processes can, consequently, also influence the development and evolution of mid-latitude cyclones and in turn also influence the formation and maintenance of atmospheric water vapor transport along ARs. Section 2.5.2 explains this concept in more detail.

## 2.5.2 Mid-Latitude Cyclones and ARs

The first modern theory for cyclone evolution originated at the Bergen School of Meteorology in the early twentieth century and is known as the Norwegian Cyclone Model (NCM; Bjerknes 1919; Bjerknes and Solberg 1922). The NCM was developed for cyclones typically located over the Northeast Atlantic, but is applicable to cyclones also located over the Northeast Pacific, and generally in regions where ARs are commonly observed (see Chap. 4). More recent studies have shown that a variety of cyclone and frontal evolutions, beyond the scope of the NCM, are possible (e.g., Browning 1990; Shapiro and Keyser 1990; Evans et al. 1994; Smigielski and Mogil 1995; Young 1995; Bosart et al. 1998; Schultz et al. 1998). The NCM (Fig. 2.17) begins with a small-scale cyclonic disturbance along the polar front that results in the advection of cold air equatorward to the west of the cyclone center, and advection of warm air poleward to the east of the cyclone center, as just described in Sect. 2.5.1. Contraction of the baroclinic zone by the temperature advection and deformation patterns results in the development of the cold and warm fronts. The cold front is observed to rotate faster than the warm front and propagates eastward, eventually catching up to the warm front. Schultz et al. (1998) showed that frontal features favor a meridional elongation and zonal contraction because the background flow is likely highly amplified and diffluent in exit region of the North Atlantic (or North Pacific) jet stream. The NCM thus describes a cyclone evolution that favors the meridional elongation of the cyclone cold front, a contraction of the thermal gradient along the cyclone cold front (i.e., frontogenesis), enhanced southerly flow in the cyclone warm sector along a LLJ stream, and a developing corridor of enhanced

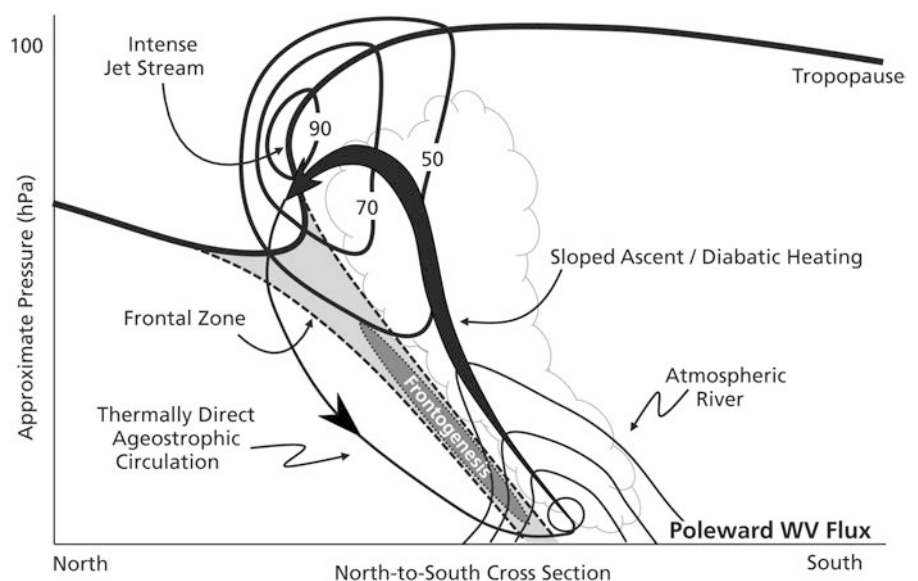
IWV and poleward water vapor flux (Lackmann 2002) that may develop into an AR. The NCM concludes with the formation of an occluded front in the region of weak baroclinicity associated with the thermal ridge that extends from the warm sector toward the cyclone center.

Observational and numerical studies show that cyclones evolve within different combinations of planetary and synoptic-scale flow configurations, variations in lower-tropospheric baroclinicity and lower-tropospheric moisture, and static stability (e.g. Bosart 1981; Reinhold and Pierrehumbert 1982; Gyakum 1983; Reed and Albright 1986; Lackmann et al. 1996; Carlson 1998). For example, the introduction of moisture and an environment with weak static stability can greatly accelerate QG forcing for (saturated) vertical motion and the cyclogenesis processes just described in Sect. 2.5.1 (see Bluestein 1992 [Eq. 5.9.28]). Cyclones may then contain large and rapidly-expanding cloud masses that illuminate likely regions of strong diabatic heating and the poleward advection of lower-tropospheric warm and moist air (e.g., Browning and Pardoe 1973; Browning 1986; Reed and Albright 1986; Wernli and Davies 1997; Schultz 2001; Martin 2006) in the possible location of an AR. This region of strong diabatic heating and latent heat release in the cyclone warm sector can have a large effect on the dynamical evolution of both the synoptic-scale and mesoscale characteristics of the developing cyclone. PV will be redistributed above and below a mid-tropospheric region of latent heat release because of the imposed vertical gradients of diabatic heating (see Martin 2006 [Eq. 9.23]). PV will therefore increase below the diabatic heating maximum and strengthen lower-tropospheric frontal zones and cyclonic circulations, whereas PV will decrease above the diabatic heating maximum, strengthening anticyclonic circulations (i.e., a shortwave ridge) aloft and enhancing the upstream upper-

level horizontal PV gradient. The strength of the frontal circulations (i.e., the cross-front ageostrophic circulations; e.g., Sawyer 1956 and Eliassen 1959) consequently increases as a result of mid-tropospheric latent heat release in the presence of weak static stability and warm and moist air (e.g., Hoskins and Bretherton 1972). This cross-front ageostrophic circulation, which may transect an AR located on the warm side of a baroclinic zone that is undergoing frontogenesis, is schematically illustrated in Fig. 2.18 by Cordeira et al. (2013). The end result of this process is a “complex interdependence” among frontal-induced precipitation, lower-tropospheric PV maxima, the LLJ, and warm-sector water vapor transport (Lackmann 2002) that can influence the structure and evolution of ARs (e.g., Sodemann and Stohl 2013; Cordeira et al. 2013).

The development of poleward water vapor transport that may form into ARs in the warm sector of the mid-latitude cyclone can, therefore, occur in conjunction with (1) processes that lead to cyclogenesis and (2) processes that lead to a modification of the ensuing cyclogenesis process. Consequently, processes that lead to modification of the cyclogenesis process in association with saturated ascent, precipitation, and latent heat release may also play a detrimental role in the maintenance and evolution of an AR (e.g., the AR’s life cycle). Maintenance of AR conditions within an Eulerian framework (i.e., local conservation of IWV or increases in the magnitude of IWV) relates a net positive or zero sum of IVT convergence, evaporation, and precipitation in the IWV budget. In the presence of precipitation, IWV is conserved in conjunction with evaporation and IVT convergence. Cordeira et al. (2013) paradoxically demonstrate that the initial formation of an AR during cyclogenesis might occur during a period with a net negative sum of the IWV budget related to a decrease in IWV via precipitation. The

**Fig. 2.18** Schematic cross-section representation of the vertical structure of a tropospheric frontal zone (dashed lines) with poleward water vapor (WV) flux (thin lower-tropospheric contours) along an AR that contains frontogenesis (shaded) and a strong thermally-direct ageostrophic circulation (counter-clockwise rotating arrow) within the equatorward entrance region of an intense tropopause-level jet stream (thick contours labeled 50, 70, and 90  $m s^{-1}$ ). (Originally modeled after Shapiro (1982) and has been adapted from Cordeira et al. 2013)



associated latent heat release, however, can profoundly affect the subsequent evolution of the synoptic-scale flow that results in an enhanced upper-tropospheric PV gradient, a stronger upper-tropospheric jet stream, and a thermally-direct (frontogenetic) ageostrophic cross-front circulation, which may subsequently aggregate IWV along the AR via IVT convergence, and offset the deleterious effect of precipitation in the IWV budget. A more robust review of water vapor budgets and water vapor source regions for ARs appeared in Sect. 2.4.

### 2.5.3 Linking Extratropical Dynamics to Hydrometeorological Effects

As discussed above (Sect. 2.5.1), RWB in the exit regions of mid-latitude jet streams—whether anticyclonic or cyclonic—can result in penetration of mid-latitude troughs into subtropical latitudes, and, in turn, enable poleward transport of water vapor along an AR in the warm sector of the mid-latitude cyclone. The type of RWB will determine the impingement angle of the water vapor transport vector along ARs on the coastal topography, modulating the intensity of orographic precipitation and the possibility of flooding over

the region. The ensuing discussion focuses on the US West Coast; however, the physical mechanisms of RWB modulation of ARs are globally applicable.

Approximately two-thirds of all detected ARs that made landfall on the US West Coast during 1979–2009 in the NASA MERRA reanalysis data set related directly to RWB over the eastern North Pacific (i.e., RWB–ARs; Hu et al. 2017). As water vapor transport along these ARs arrives at the coast, it encounters the topography of the region: the north-to-south-oriented Cascade Range of the Pacific Northwest or the northwest-to-southeast-oriented Sierra Nevada or Coast Range of California. The impinging angle of the water vapor transport vector on topography can critically determine the intensity of orographic precipitation and the flooding of the affected watersheds (Ralph et al. 2003; Neiman et al. 2011). As expected, the impinging angles of the water vapor transport vector along ARs associated with anticyclonic wave breaking (i.e., AWB–ARs) and cyclonic wave breaking (i.e., CWB–ARs) are very different, as exemplified for the Pacific Northwest US (Fig. 2.19b). Landfalling CWB–ARs over the Pacific Northwest USA predominantly contain water vapor transport that impinges on topography at angles between  $10^\circ$  and  $70^\circ$ , with a median of  $36^\circ$  (i.e., associated with a south-southwesterly IVT direction; Fig. 2.19b),

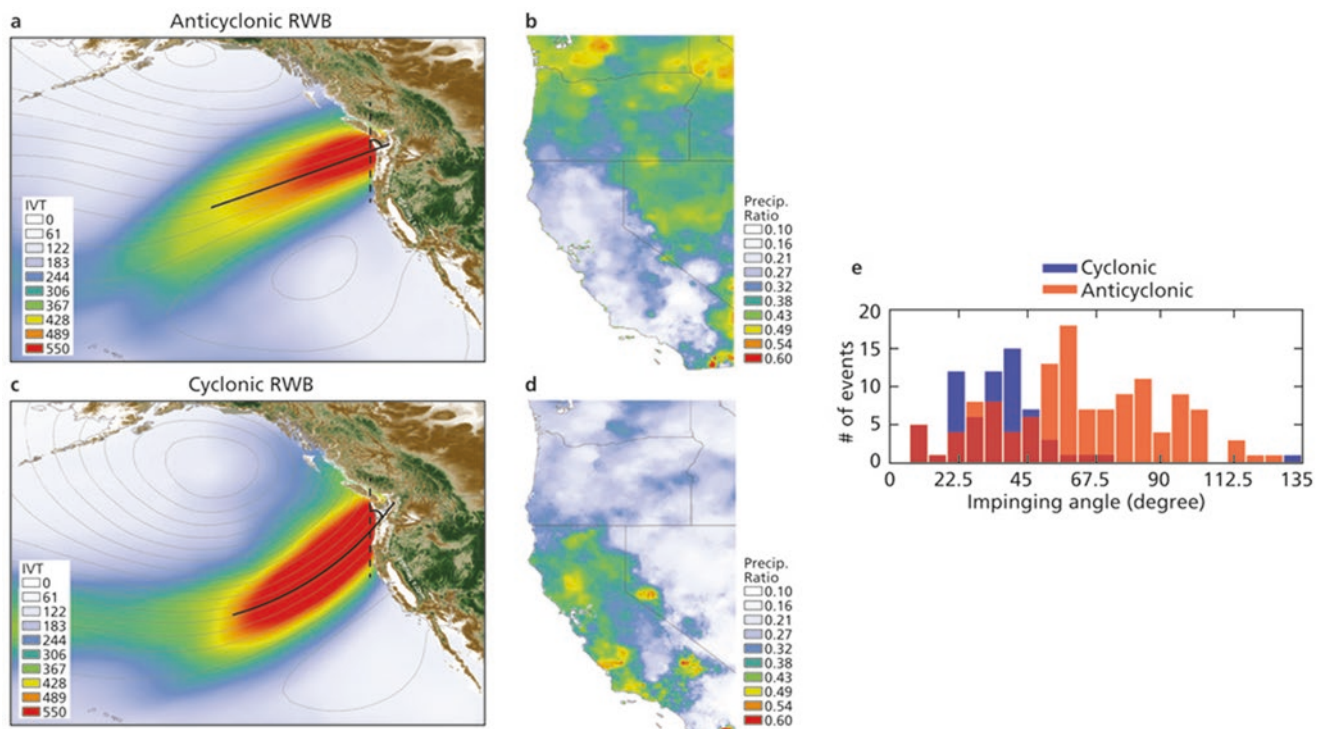


**Fig. 2.19** (a, b) IVT (shaded according to scale:  $\text{kg m}^{-1} \text{s}^{-1}$ ) and 875-hPa geopotential height (dashed contours; m) composites for all AWB–ARs and CWB–ARs that impinge on the Pacific Northwest US Coast ( $44\text{--}49^\circ\text{N}$ ). The blue line is the average location of the IVT axis extending upstream 2000 km, whereas the dashed blue lines indicate  $\pm 1$  stan-

dard deviation in the average location for the IVT axis. (c, d) Ratio of AR-related precipitation from all AWB–ARs and CWB–ARs to all AR-related precipitation for all US West Coast locations ( $36\text{--}49^\circ\text{N}$ ). (Image adapted from Hu et al. 2017)

whereas AWB-ARs contain a broader range and a median angle of  $62^\circ$  (i.e., associated with a west-southwesterly IVT direction; Fig. 2.19a). These different impinging angles influence the topographically-modulated AR-related precipitation.

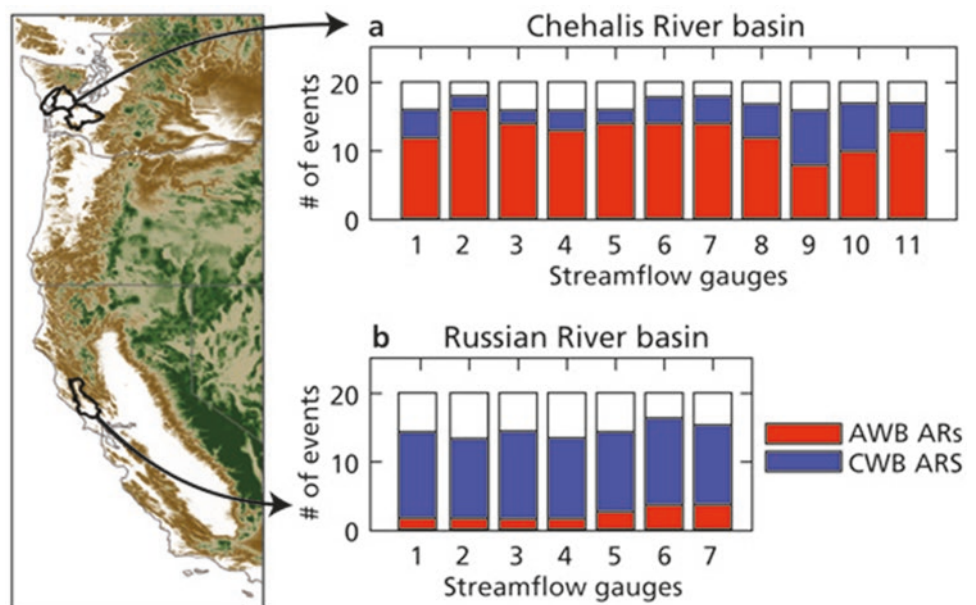
Along the Pacific Northwest US Coast (e.g., Washington and Oregon) and some mountainous regions of the Pacific Southwest US Coast (e.g., California), more than 70% of total AR-related precipitation results from RWB-ARs (not shown; see Hu et al. 2017). Interestingly, when the precipitation related to AWB-ARs or CWB-ARs is isolated, a clear pattern emerges. The Pacific Northwest US Coast is predominantly affected by AWB-ARs, which account for more than 40% of AR-related precipitation (Fig. 2.19c). In contrast, a larger portion of AR-related precipitation in the Pacific Southwest US Coast is associated with CWB-ARs (Fig. 2.19d). Clearly, from these results, intense precipitation preferentially occurs over mountains ranges where the water vapor transport vector along an AR is oriented parallel to the upslope terrain vector. These sharp differences in AR-related precipitation associated with AWB and CWB result in significant differences in streamflow. Hu et al. (2017) analyzed the 20 most intense AR-related streamflow events in the Chehalis River basin in western Washington, and the Russian River basin in northern California. The analysis found that AWB-ARs play a dominant role in explaining the top streamflow events measured within the Chehalis, while CWB-ARs were responsible for most of the top streamflow events in the Russian River basin (Fig. 2.20). It is important to emphasize that many other factors—including antecedent soil moisture conditions, the phase of precipitation (liquid or solid), and the response of the watershed—will all influ-

ence the streamflow response. In the case of the Chehalis River basin, AWB-ARs affect the basin more frequently and are also associated with more precipitation falling in liquid rather than snow form.

### 2.5.4 Summary

The mid-latitude storm track comprises synoptic-scale eddies that are characterized by Rossby waves. These Rossby waves can sometimes penetrate into the subtropics where they may initiate poleward water vapor transport that could serve as the impetus for AR formation. Alternatively, these Rossby waves may also initiate cyclogenesis in the presence of favorable synoptic-scale conditions that relate to the vertical structure of the atmosphere, moisture content, and static stability. The horizontal circulations associated with mid-latitude cyclogenesis may further contribute to poleward water vapor transport and the initial formation of an AR in the warm sector of a cyclone. This warm sector of the cyclone is characterized by enhanced water vapor and weak static stability that can play a crucial role in cyclone intensification related to saturated ascent, precipitation, and diabatic heating. These can, in turn, influence the evolution and strength of frontal circulations and ARs. As such, cyclones can simultaneously deplete IWV along the AR via precipitation in the presence of saturated ascent and generate IWV along the AR via IVT convergence in the presence of frontogenesis. This generation and depletion of IWV along an AR modulates the AR life cycle, which is intimately related to the life cycle of the mid-latitude cyclone, the evolution of the large-scale flow, and the dynamical processes related to precipitation. In fact, mid-latitude dynamics, as characterized by the different

**Fig. 2.20** Number of top 20 streamflow events to AWB-ARs (red) and CWB-ARs (blue) for each gauge within the (a) Chehalis River basin and (b) the Russian River basin (Hu et al. 2017)



types of RWB, can modulate the spatial pattern and intensity of precipitation and streamflow on the US West Coast.

Improved understanding of AR-related large-scale dynamics and associated hydrologic effects could improve prediction skill. The inter-annual variability of RWB over the Northeast Pacific is modulated in part by the El Niño–Southern Oscillation (ENSO), because the number of AWB events is higher during La Niña years, while CWB is higher during El Niño (Ryoo et al. 2013). Furthermore, climate change could modify RWB dynamics. In fact, Barnes and Hartmann (2012) found a poleward shift of RWB events and a significant decrease of CWB events as a result of poleward shift of mid-latitude jets under increased greenhouse gas forcing. How these changes could affect both large-scale atmospheric dynamics and local hydrology is an important topic for future research.

## 2.6 A Case Study Example

As an illustration of the three features and their linkage, Fig. 2.5 shows a North Atlantic cyclone in November 1992. This cyclone formed as a frontal wave at 0000 UTC 22 November on a meridionally elongated cold front, downstream of a pronounced, narrow, and elongated upper-level trough, and then experienced rapid intensification from the strong vertical coupling of the upper-level trough and the low-level disturbance. Eventually, at 0000 UTC 24 November, the system became a mature, deep, and stationary Icelandic Low (see the detailed discussions in Wernli (1997) and Rossa et al. (2000)). Figure 2.5 illustrates the development of this cyclone in terms of the sea-level pressure field and the superimposed, objectively identified TMEs, ARs, and WCBs.

At 00 UTC 22 November, an elongated AR (red shading in Fig. 2.5a) extends from the Caribbean Sea over the cyclogenesis area near 30°W, 40°N (see label *L*) to Western Europe. Most of this AR overlaps with WCB trajectories (blue contours mark the outline of WCB trajectory positions at this time), while a TME feature exiting from the tropics between 30° and 40°W only partially overlaps with the AR. This indicates that at this time the AR air masses are mainly of extratropical origin (otherwise, the overlap with the TME would be larger) and that strong ascent occurs along the AR. One day later (Fig. 2.5b), the cyclone intensifies and is now located near 16°W, 56°N. An elongated and strongly bent AR still extends from 30°N along the cold front to the cyclone center and then eastward along the warm front into Central Europe. At this time, the AR agrees well with TME trajectories along the cold-frontal part, and a large WCB bends from the cyclone's warm sector to the north of the extended warm front. Evidently, a substantial part of the pre-cold-frontal AR at this time is of tropical origin, and the

almost parallel and only weakly overlapping arrangement of the three features along the warm front points to the non-trivial relative motion of their associated air parcels. One day later (Fig. 2.5c), the cyclone has attained a central sea-level pressure of about 960 hPa near Iceland. Along its cold front, extending from 35°N to Scandinavia, a narrow AR coincides almost perfectly with a TME which extends further poleward. The WCB related to this cyclone is now fully detached from the AR and TME features and extends from Greenland to Finland near 70°N.

This brief case study thus illustrates the complex relationship of the three flow features, in this case with an AR that is first well aligned with a WCB and later with a TME. The WCB mainly highlights the region where moist air ascends in the frontal regions of the cyclone, the AR emphasizes the strong filamentary poleward moisture transport mainly in the cyclone's warm sector, and the TME reveals that some of the air that contributes to the strong water vapor transport in the AR and the rain-out in the WCB is actually of tropical origin.

**Acknowledgements** We are most grateful to Hanin Binder, Maxi Boettcher, Hanna Joos, Erica Madonna, Gregor Pante, and Michael Sprenger for their support in establishing the ERA-Interim climatologies of WCBs and TMEs. We also thank MeteoSwiss for granting access to ECMWF data, and Paul Neiman and Duane Waliser for their very supportive and constructive reviews.

## References

- Anderson BT, Strahler AH (2008) Visualizing weather and climate. Wiley, Hoboken
- Appenzeller C, Davies HC (1992) Structure of stratospheric intrusions into the troposphere. *Nature* 358:570–572. <https://doi.org/10.1038/358570a0>
- Bao J-W, Michelson SA, Neiman FM et al (2006) Interpretation of enhanced integrated water vapor bands associated with extratropical cyclones: their formation and connection to tropical moisture. *Mon Weather Rev* 134:1063–1080. <https://doi.org/10.1175/mwr3123.1>
- Barnes EA, Hartmann DL (2012) Detection of Rossby wave breaking and its response to shifts of the midlatitude jet with climate change. *J Geophys Res* 117:D09117. <https://doi.org/10.1029/2012jd017469>
- Bjerknes J (1919) on the structure of moving cyclones. *Mon Weather Rev* 47:95–99. [https://doi.org/10.1175/1520-0493\(1919\)47<95:otsomc>2.0.co;2](https://doi.org/10.1175/1520-0493(1919)47<95:otsomc>2.0.co;2)
- Bjerknes J, Solberg H (1922) Life cycle of cyclones and the polar front theory of atmospheric circulation. *Geophys Publ* 3:3–18
- Bluestein H (1992) Synoptic-dynamic meteorology in midlatitudes. Oxford University Press, Oxford
- Bonne J-L et al (2015) The summer 2012 Greenland heat wave: in situ and remote sensing observations of water vapor isotopic composition during an atmospheric river event. *J Geophys Res* 120(7):2970–2989
- Bosart LF (1981) The presidents' day snowstorm of 18–19 February 1979: a subsynoptic-scale event. *Mon Weather Rev* 109:1542–1566. [https://doi.org/10.1175/1520-0493\(1981\)109<1542:tpdsof>2.0.co;2](https://doi.org/10.1175/1520-0493(1981)109<1542:tpdsof>2.0.co;2)
- Bosart LF, Bracken WE, Seimon A (1998) A Study of cyclone mesoscale structure with emphasis on a large-amplitude inertia–

- gravity wave. *Mon Weather Rev* 126:1497–1527. [https://doi.org/10.1175/1520-0493\(1998\)126<1497:asocms>2.0.co;2](https://doi.org/10.1175/1520-0493(1998)126<1497:asocms>2.0.co;2)
- Bowman KP, Lin JC, Stohl A et al (2013) Input data requirements for Lagrangian trajectory models. *Bull Am Meteorol Soc* 94:1051–1058. <https://doi.org/10.1175/BAMS-D-12-00076.1>
- Browning KA (1971) Radar measurements of air motion near fronts. Part two: some categories of frontal air motion. *Weather* 26:320–340
- Browning KA (1986) Conceptual models of precipitation systems. *Wea Forecast* 1:23–41. [https://doi.org/10.1175/1520-0434\(1986\)001<0023:cmops>2.0.co;2](https://doi.org/10.1175/1520-0434(1986)001<0023:cmops>2.0.co;2)
- Browning KA (1990) Organization of clouds and precipitation in extratropical cyclones. In: Newton CW, Holopainen EO (eds) *Extratropical cyclones: the Erik Palmén memorial volume*. American Meteorological Society, Boston, pp 129–153
- Browning KA, Harrold TW (1969) Air motion and precipitation growth in a wave depression. *Q J R Meteorol Soc* 95:288–309
- Browning KA, Pardoe CW (1973) Structure of low-level jet streams ahead of mid-latitude cold fronts. *Q J R Meteorol Soc* 99:619–638. <https://doi.org/10.1256/smsqj.42203>
- Carlson TN (1980) Airflow through midlatitude cyclones and the comma cloud pattern. *Mon Weather Rev* 108:1498–1509
- Carlson TN (1998) Mid-latitude weather systems. American Meteorological Society, Boston, p 507
- Coplen TB, Neiman PJ, White AB et al (2008) Extreme changes in stable hydrogen isotopes and precipitation characteristics identified in a land-falling Pacific storm using a novel precipitation collector and meteorological observatory. *Geophys Res Lett* 35:L21808. <https://doi.org/10.1029/2008GL035481>
- Coplen TB, Neiman PJ, White AB et al (2015) Categorization of northern California rainfall for periods with and without a radar bright-band using stable isotopes and a novel automated precipitation collector. *Tellus B* 67:48. <https://doi.org/10.3402/tellusb.v67.28574>
- Cordeira JM, Ralph FM, Moore BJ (2013) The development and evolution of two atmospheric rivers in proximity to Western North Pacific tropical cyclones in October 2010. *Mon Weather Rev* 141:4234–4255. <https://doi.org/10.1175/mwr-d-13-00019.1>
- Dacre HF, Clark PA, Martinez-Alvarado O et al (2015) How do atmospheric rivers form? *Bull Am Meteorol Soc* 96:1243–1255
- Davies HC (1997) Emergence of the mainstream cyclogenesis theories. *Meteor Z* 6:261–274
- Dee DP et al (2011) The ERA-interim reanalysis: configuration and performance of the data assimilation system. *Q J R Meteorol Soc* 137:553–597
- Eckhardt S, Stohl A, Wernli H et al (2004) A 15-year climatology of warm conveyor belts. *J Clim* 17:218–237
- Eliassen A (1959) On the formation of fronts in the atmosphere, The Rossby Memorial Volume. Rockefeller Institute Press, New York
- Ertel H (1942) Ein neuer hydrodynamischer Erhaltungssatz. *Die Naturwissenschaften* 30:543–544. <https://doi.org/10.1007/bf01475602>
- Evans MS, Keyser D, Bosart LF et al (1994) A satellite-derived classification scheme for rapid maritime cyclogenesis. *Mon Weather Rev* 122:1381–1416. [https://doi.org/10.1175/1520-0493\(1994\)122<1381:asdcfs>2.0.co;2](https://doi.org/10.1175/1520-0493(1994)122<1381:asdcfs>2.0.co;2)
- Fröhlich L, Knippertz P, Fink AH et al (2013) An objective climatology of tropical plumes. *J Clim* 26:5044–5060. <https://doi.org/10.1175/JCLI-D-12-00351.1>
- Grams CM, Wernli H, Boettcher M et al (2011) The key role of diabatic processes in modifying the upper-tropospheric wave guide: a North Atlantic case-study. *Q J R Meteorol Soc* 137:2174–2193
- Green JSA, Ludlam FH, McIlveen JFR (1966) Isentropic relative-flow analysis and the parcel theory. *Q J R Meteorol Soc* 92:210–219
- Guan B, Waliser DE (2015) Detection of atmospheric rivers: evaluation and application of an algorithm for global studies. *J Geophys Res Atmos* 120:12514–12535. <https://doi.org/10.1002/2015JD024257>
- Guan B, Waliser D, Ralph FM (2018) An Inter-comparison between reanalysis and dropsonde observations of the total water vapor transport in individual atmospheric rivers. *J Hydrometeorol* 19(2):321–337. <https://doi.org/10.1175/JHM-D-17-0114.1>
- Gyakum JR (1983) On the evolution of the QE II storm. II: dynamic and thermodynamic structure. *Mon Weather Rev* 111:1156–1173. [https://doi.org/10.1175/1520-0493\(1983\)111<1156:oteoti>2.0.co;2](https://doi.org/10.1175/1520-0493(1983)111<1156:oteoti>2.0.co;2)
- Holton JR (2004) *An introduction to dynamic meteorology*. Elsevier, Amsterdam
- Hoskins BJ, Bretherton FP (1972) Atmospheric frontogenesis models: mathematical formulation and solution. *J Atmos Sci* 29:11–37. [https://doi.org/10.1175/1520-0469\(1972\)029<0011:afmmfa>2.0.co;2](https://doi.org/10.1175/1520-0469(1972)029<0011:afmmfa>2.0.co;2)
- Hoskins BJ, McIntyre ME, Robertson AW (1985) On the use and significance of isentropic potential vorticity maps. *Q J R Meteorol Soc* 111:877–946. <https://doi.org/10.1256/smsqj.47001>
- Hu H, Dominguez F, Wang Z et al (2017) Linking atmospheric river hydrological impacts on the U.S. west coast to Rossby wave breaking. *J Clim* 30:3381–3399. <https://doi.org/10.1175/JCLI-D-16-0386.1>
- Joos H, Wernli H (2012) Influence of microphysical processes on the potential vorticity development in a warm conveyor belt: a case study with the limited area model COSMO. *Q J R Meteorol Soc* 138:407–418
- Jouzel J, G. Delaygue, A. Landais, V. Masson-Delmotte, C. Risi, and F. Vimeux (2013), Water isotopes as tools to document oceanic sources of precipitation, *Water Resour. Res.*, 49, 7469–7486, <https://doi.org/10.1002/2013WR013508>
- Knippertz P (2007) Tropical–extratropical interactions related to upper-level troughs at low latitudes. *Dyn Atmos Oceans* 43:36–62. <https://doi.org/10.1016/j.dynatmoce.2006.06.003>
- Knippertz P, Martin JE (2005) Tropical plumes and extreme precipitation in subtropical and tropical West Africa. *Q J R Meteorol Soc* 131:2337–2365. <https://doi.org/10.1256/qj.04.148>
- Knippertz P, Martin JE (2007) A Pacific moisture conveyor belt and its relationship to a significant precipitation event in the semi-arid southwestern United States. *Wea Forecast* 22:125–144. <https://doi.org/10.1175/WAF963.1>
- Knippertz P, Wernli H (2010) A Lagrangian climatology of tropical moisture exports to the Northern Hemispheric extratropics. *J Clim* 23:987–1003. <https://doi.org/10.1175/2009JCLI3333.1>
- Knippertz P, Wernli H, Gläser G (2013) A global climatology of tropical moisture exports. *J Clim* 26:3031–3045. <https://doi.org/10.1175/JCLI-D-12-00401.1>
- Lackmann GM (2002) Cold-frontal potential vorticity maxima, the low-level jet, and moisture transport in extratropical cyclones. *Mon Weather Rev* 130:59–74. [https://doi.org/10.1175/1520-0493\(2002\)130<0059:cfpvm>2.0.co;2](https://doi.org/10.1175/1520-0493(2002)130<0059:cfpvm>2.0.co;2)
- Lackmann GM, Bosart LF, Keyser D (1996) Planetary- and synoptic-scale characteristics of explosive wintertime cyclogenesis over the Western North Atlantic ocean. *Mon Weather Rev* 124:2672–2702. [https://doi.org/10.1175/1520-0493\(1996\)124<2672:passco>2.0.co;2](https://doi.org/10.1175/1520-0493(1996)124<2672:passco>2.0.co;2)
- Läderach A, Sodemann H (2016) A revised picture of the atmospheric moisture residence time. *Geophys Res Lett* 43:924–933. <https://doi.org/10.1002/2015GL067449>
- Lau WKM, Waliser DE, Waliser D (2011) Predictability and forecasting. In: *Intraseasonal variability in the atmosphere-ocean climate system*. Springer, Berlin, pp 433–476. [https://doi.org/10.1007/978-3-642-13914-7\\_12](https://doi.org/10.1007/978-3-642-13914-7_12)
- Lorenz EN (1955) Available potential energy and the maintenance of the general circulation. *Tellus* 7:157–167. <https://doi.org/10.1111/j.2153-3490.1955.tb01148.x>
- Lu M, Lall U, Schwartz A et al (2013) Precipitation predictability associated with tropical moisture exports and circulation patterns for a

- major flood in France in 1995. *Water Resour Res* 49:6381–6392. <https://doi.org/10.1002/wrcr.20512>
- Madonna E, Wernli H, Joos H et al (2014) Warm conveyor belts in the ERA-Interim data set (1979–2010). Part I: Climatology and potential vorticity evolution. *J Clim* 27:3–26
- Martin JE (2006) *Mid-latitude atmospheric dynamics: a first course*. Wiley, Chichester
- Matthews AJ, Kiladis GN (1999) The tropical–extratropical interaction between high-frequency transients and the Madden–Julian oscillation. *Mon Weather Rev* 127:661–677. [https://doi.org/10.1175/1520-0493\(1999\)127<0661:tteibh>2.0.co;2](https://doi.org/10.1175/1520-0493(1999)127<0661:tteibh>2.0.co;2)
- McElroy MB (2002) *The atmospheric environment: effects of human activity*. Princeton University Press, Princeton
- McGuirk JP, Thompson AH, Smith NR (1987) Moisture bursts over the tropical pacific ocean. *Mon Weather Rev* 115:787–798. [https://doi.org/10.1175/1520-0493\(1987\)115<0787:mbottp>2.0.co;2](https://doi.org/10.1175/1520-0493(1987)115<0787:mbottp>2.0.co;2)
- McGuirk JP, Thompson AH, Schaefer JR (1988) An Eastern pacific tropical plume. *Mon Weather Rev* 116:2505–2521. [https://doi.org/10.1175/1520-0493\(1988\)116<2505:aeptp>2.0.co;2](https://doi.org/10.1175/1520-0493(1988)116<2505:aeptp>2.0.co;2)
- Miller ST (2015) *Applied thermodynamics for meteorologists*. Cambridge University Press, Cambridge
- Miltenberger AK, Pfahl S, Wernli H (2013) An online trajectory module (version 1.0) for the nonhydrostatic numerical weather prediction model COSMO. *Geosci Model Dev* 6:1989–2004. <https://doi.org/10.5194/gmd-6-1989-2013>
- Moore RW, Martini O, Spengler T (2010) The Modulation of the subtropical and extratropical atmosphere in the pacific basin in response to the Madden–Julian oscillation. *Mon Weather Rev* 138:2761–2779. <https://doi.org/10.1175/2010mwr3194.1>
- Neiman PJ, Schick LJ, Ralph FM et al (2011) Flooding in Western Washington: the connection to atmospheric rivers. *J Hydrometeorol* 12:1337–1358. <https://doi.org/10.1175/2011jhm1358.1>
- Newell RE, Newell NE, Zhu Y et al (1992) Tropospheric rivers? - A pilot study. *Geophys Res Lett* 19:2401–2404. <https://doi.org/10.1029/92gl02916>
- Newman M, Kiladis GN, Weickmann KM et al (2012) Relative contributions of synoptic and low-frequency eddies to time-mean atmospheric moisture transport, including the role of atmospheric rivers. *J Clim* 25:7341–7361. <https://doi.org/10.1175/jcli-d-11-00665.1>
- Payne AE, Magnusdotir G (2014) Dynamics of landfalling atmospheric rivers over the north pacific in 30 years of MERRA reanalysis. *J Clim* 27:7133–7150. <https://doi.org/10.1175/jcli-d-14-00034.1>
- Persson POG, Neiman, PJ, Walter B et al (2005) Contributions from California coastal-zone surface fluxes to heavy coastal precipitation: A CALJET case study During the Strong El Niño of 1998. *Mon Wea Rev* 133:1175–1198
- Pettersen S, Smebye SJ (1971) On the development of extratropical cyclones. *Q J Roy Met Soc* 97:457–482. <https://doi.org/10.1002/qj.49709741407>
- Pfahl S, Madonna E, Boettcher M et al (2014) Warm conveyor belts in the ERA-Interim data set (1979–2010). Part II: Moisture origin and relevance for precipitation. *J Clim* 27:27–40
- Pfahl S, Schwierz C, Croci-Maspoli M et al (2015) Importance of latent heat release in ascending air streams for atmospheric blocking. *Nat Geosci* 8:610–615
- Ralph FM, Neiman PJ, Kingsmill DE et al (2003) The impact of a prominent rain shadow on flooding in California’s Santa Cruz mountains: A CALJET Case Study and sensitivity to the ENSO cycle. *J Hydrometeorol* 4:1243–1264. [https://doi.org/10.1175/1525-7541\(2003\)004<1243:tioapr>2.0.co;2](https://doi.org/10.1175/1525-7541(2003)004<1243:tioapr>2.0.co;2)
- Ralph MF, Neiman PJ, Wick GA (2004) Satellite and CALJET aircraft observations of atmospheric rivers over the eastern North pacific ocean during the winter of 1997/98. *Mon Weather Rev* 132:1721–1745
- Ralph FM, Neiman PJ, Kiladis GN et al (2011) A multiscale observational case study of a Pacific atmospheric river exhibiting tropical–extratropical connections and a mesoscale frontal wave. *Mon Weather Rev* 139:1169–1189
- Ralph FM, Iacobellus SF, Neiman PJ et al (2017a) Dropsonde observations of total water vapor transport within North Pacific atmospheric rivers. *J Hydrometeorol* 18:2577–2596
- Ralph FM, Dettinger M, Lavers D et al (2017b) Atmospheric rivers emerge as a global science and applications focus. *Bull Am Meteorol Soc* 98:1969–1973. <https://doi.org/10.1175/BAMS-D-16-0262.1>
- Ralph FM, Dettinger MD, Cairns MM et al (2018) Defining “atmospheric river”: how the glossary of meteorology helped resolve a debate. *Bull Am Meteorol Soc* 99:837–839. <https://doi.org/10.1175/BAMS-D-17-0157.1>
- Reed RJ, Albright MD (1986) A case study of explosive cyclogenesis in the Eastern Pacific. *Mon Weather Rev* 114:2297–2319. [https://doi.org/10.1175/1520-0493\(1986\)114<2297:acsoec>2.0.co;2](https://doi.org/10.1175/1520-0493(1986)114<2297:acsoec>2.0.co;2)
- Reinhold BB, Pierrehumbert RT (1982) Dynamics of weather regimes: quasi-stationary waves and blocking. *Mon Weather Rev* 110:1105–1145. [https://doi.org/10.1175/1520-0493\(1982\)110<1105:dowrqs>2.0.co;2](https://doi.org/10.1175/1520-0493(1982)110<1105:dowrqs>2.0.co;2)
- Rossa AM, Wernli H, Davies HC (2000) Growth and decay of an extratropical cyclone’s PV-tower. *Meteorog Atmos Phys* 73:139–156
- Rossby CG et al (1937) Isentropic analysis. *Bull Am Meteorol Soc* 18:201–209
- Rutz JJ, Steenburgh WJ, Ralph FM (2014) Climatological characteristics of atmospheric rivers and their inland penetration over the western United States. *Mon Weather Rev* 142:905–921
- Rutz JJ, Steenburgh WJ, Ralph FM (2015) The inland penetration of atmospheric rivers over western North America: a Lagrangian analysis. *Mon Weather Rev* 143:1924–1944
- Ryoo J-M, Kaspi Y, Waugh DW et al (2013) Impact of Rossby wave breaking on U.S. west coast winter precipitation during ENSO events. *J Clim* 26:6360–6382. <https://doi.org/10.1175/jcli-d-12-00297.1>
- Ryoo J-M, Waliser DE, Waugh DW et al (2015) Classification of atmospheric river events on the U.S. West Coast using a trajectory model. *J Geophys Res* 120:3007–3028. <https://doi.org/10.1002/2014JD022023>
- Sawyer JS (1956) The vertical circulation at meteorological fronts and its relation to frontogenesis. *Proc Roy Soc London A* 234:346–362
- Schultz DM (2001) Reexamining the cold conveyor belt. *Mon Weather Rev* 129:2205–2225. [https://doi.org/10.1175/1520-0493\(2001\)129<2205:RTCCB>2.0.CO;2](https://doi.org/10.1175/1520-0493(2001)129<2205:RTCCB>2.0.CO;2)
- Schultz DM, Keyser D, Bosart LF (1998) The effect of large-scale flow on low-level frontal structure and evolution in midlatitude cyclones. *Mon Weather Rev* 126:1767–1791. [https://doi.org/10.1175/1520-0493\(1998\)126<1767:teolsf>2.0.co;2](https://doi.org/10.1175/1520-0493(1998)126<1767:teolsf>2.0.co;2)
- Shapiro MA (1982) *Mesoscale weather systems of the central United States*. University of Colorado, Boulder, p 78
- Shapiro MA, Keyser D (1990) Fronts, jet streams and the tropopause. In: Newton CW, Holopainen EO (eds) *Extratropical cyclones: the Erik Palmén memorial volume*. Amer Meteor Soc, Boston, pp 167–191
- Shaw WN, Lempfert RGK (1906) The life history of surface air currents. A study of the surface trajectories of moving air. Meteor. Office Memoir No. 174, reprinted in: *Selected Meteorological Papers of Sir Napier Shaw*. Macdonald, 1955, pp 15–131
- Smigielski FJ, Mogil HM (1995) A systematic satellite approach for estimating central surface pressures of mid-latitude cold season oceanic cyclones. *Tellus A*. <https://doi.org/10.3402/tellusa.v47i5.11581>
- Sodemann H, Stohl A (2013) Moisture origin and meridional transport in atmospheric rivers and their association with multiple cyclones. *Mon Weather Rev* 141:2850–2868. <https://doi.org/10.1175/mwr-d-12-00256.1>

- Sodemann H, Schwierz C, Wernli H (2008a) Interannual variability of Greenland winter precipitation sources: Lagrangian moisture diagnostic and North Atlantic Oscillation influence. *J Geophys Res* 113:D03107
- Sodemann H, Masson-Delmotte M, Schwierz C et al (2008b) Interannual variability of Greenland winter precipitation sources. 2. Effects of North Atlantic Oscillation variability on stable isotopes in precipitation. *J Geophys Res* 113:D12111
- Steinschneider S, Lall U (2016) Spatiotemporal structure of precipitation related to tropical moisture exports over the eastern United States and its relation to climate teleconnections. *J Hydrometeorol* 17:897–913. <https://doi.org/10.1175/JHM-D-15-0120.1>
- Stohl A (2001) A 1-year Lagrangian “climatology” of airstreams in the Northern Hemisphere troposphere and lowermost stratosphere. *J Geophys Res* 106(D7):7263–7279
- Stohl A, James P (2004) A Lagrangian analysis of the atmospheric branch of the global water cycle. Part I: method description, validation, and demonstration for the August 2002 flooding in Central Europe. *J Hydrometeorol* 5(8):656–678
- Stohl A, Forster C, Sodemann H (2008) Remote sources of water vapor forming precipitation on the Norwegian west coast at 60°N – a tale of hurricanes and an atmospheric river. *J Geophys Res* 113:D05102. <https://doi.org/10.1029/2007JD009006>
- Sutcliffe RC (1939) Cyclonic and anticyclonic development. *Q J R Meteorol Soc* 65:518–524. <https://doi.org/10.1002/qj.49706528208>
- Sutcliffe RC (1947) A contribution to the problem of development. *Q J R Meteorol Soc* 73:370–383. <https://doi.org/10.1002/qj.49707331710>
- Sutcliffe RC, Forsdyke AG (1950) The theory and use of upper air thickness patterns in forecasting. *Q J R Meteorol Soc* 76:189–217. <https://doi.org/10.1002/qj.49707632809>
- Thorncroft C, Hoskins B, McIntyre M (1993) Two paradigms of baroclinic-wave life-cycle behaviour. *Q J R Meteorol Soc* 119:17–55. <https://doi.org/10.1256/smsqj.50902>
- Trenberth KE (1978) On the interpretation of the diagnostic quasi-geostrophic omega equation. *Mon Weather Rev* 106:131–137. [https://doi.org/10.1175/1520-0493\(1978\)106<0131:OTIOTD>2.0.CO;2](https://doi.org/10.1175/1520-0493(1978)106<0131:OTIOTD>2.0.CO;2)
- Webster PJ, Holton JR (1982) Cross-equatorial response to middle-latitude forcing in a zonally varying basic state. *J Atmos Sci* 39:722–733. [https://doi.org/10.1175/1520-0469\(1982\)039<0722:CERTML>2.0.CO;2](https://doi.org/10.1175/1520-0469(1982)039<0722:CERTML>2.0.CO;2)
- Wernli H (1997) A Lagrangian-based analysis of extratropical cyclones. II: a detailed case study. *Q J R Meteorol Soc* 123:1677–1706
- Wernli H, Davies HC (1997) A Lagrangian-based analysis of extratropical cyclones. I: the method and some applications. *Q J R Meteorol Soc* 123:467–489. <https://doi.org/10.1002/qj.49712353811>
- Wernli H, Schwierz C (2006) Surface cyclones in the ERA40 data set (1958–2001). Part I: novel identification method and global climatology. *J Atmos Sci* 63:2486–2507
- Winschall A, Pfahl S, Sodemann H et al (2014) Comparison of Eulerian and Lagrangian moisture source diagnostics – the flood event in eastern Europe in May 2010. *Atmos Chem Phys* 14:6605–6619. <https://doi.org/10.5194/acp-14-6605-2014>
- Woods C, Caballero R, Svensson G (2013) Large-scale circulation associated with moisture intrusions into the Arctic during winter. *Geophys Res Lett* 40:4717–4721. <https://doi.org/10.1002/grl.50912>
- Yoshimura K, Kanamitsu M, Dettlinger M (2010) Regional downscaling for stable water isotopes: a case study of an atmospheric river event. *J Geophys Res* 115:D18114. <https://doi.org/10.1029/2010JD014032>
- Young MV (1995) Types of cyclogenesis. In: Bader MJ, Forbes GS, Grant JR, Lilley RBE, Waters AJ (eds) *Images in weather forecasting*. Cambridge University Press, Cambridge, pp 213–286
- Zhu Y, Newell RE (1994) Atmospheric rivers and bombs. *Geophys Res Lett* 21(18):1999–2002
- Zhu Y, Newell RE (1998) A proposed algorithm for moisture fluxes from atmospheric rivers. *Mon Weather Rev* 126:725–735. [https://doi.org/10.1175/1520-0493\(1998\)126<0725:APAFMF>2.0.CO;2](https://doi.org/10.1175/1520-0493(1998)126<0725:APAFMF>2.0.CO;2)

## Repository KITopen

Dies ist ein Postprint/begutachtetes Manuskript.

Empfohlene Zitierung:

Sodemann, H.; Wernli, H.; Knippertz, P.; Cordeira, J. M.; Dominguez, F.; Guan, B.; Hu, H.; Ralph, F. M.; Stohl, A.

[Structure, Process, and Mechanism.](#)

2020. Atmospheric Rivers. Ed.: F.M. Ralph.

doi: [10.5445/IR/1000122540](https://doi.org/10.5445/IR/1000122540)

Zitierung der Originalveröffentlichung:

Sodemann, H.; Wernli, H.; Knippertz, P.; Cordeira, J. M.; Dominguez, F.; Guan, B.; Hu, H.; Ralph, F. M.; Stohl, A.

[Structure, Process, and Mechanism.](#)

2020. Atmospheric Rivers. Ed.: F.M. Ralph, 15–43, Springer International Publishing.

doi: [10.1007/978-3-030-28906-5\\_2](https://doi.org/10.1007/978-3-030-28906-5_2)

Lizenzinformationen: [KITopen-Lizenz](#)